PHYSICS OF DIFFUSE OPTICAL IMAGING

by

Nasire Uluç

B.S., Physics, Trakya University, 2008

Submitted to the Institute for Graduate Studies in
Science and Engineering in partial fulfillment of
the requirements for the degree of
Master of Science

Graduate Program in Physics

Boğaziçi University

2012

ACKNOWLEDGEMENTS

I would like to thank to my thesis advisor Assoc. Prof. Mehmet Burçin Ünlü for his support, encouragement, foresight, and guidance, throughout my M.S thesis study. Without his motivations and enthusiasm, it would not have been possible to write the thesis.

I would like to thank Hakan Erkol for valuable guidance and constructive feedback greatly contributing to this thesis. I have learned a lot from him.

I would like to thank to Aytaç Demirkıran and Esra Aytaç Kipergil for helpful discussion when I was writing this thesis. I am also thankful to all of my group of friends, Şirin Yonucu, Deniz Öztürk, Ümit Arabul, Duygu Kaba, for a friendly atmosphere and patiently sharing their abundance of knowledge.

I would like to thank my sincere friends Pınar Kütükçü and Zehra Öztürk for their support and patience for all my graduate education.

Finally, I am particulary indebted to my family for their support and patience during my education.

ABSTRACT

PHYSICS OF DIFFUSE OPTICAL IMAGING

Diffuse optical tomography (DOT) is a functional imaging modality which consists of transilluminating of a volume. This diagnosis technique is particulary useful for characterizing thick tissue especially for breast tissue. By using model based image reconstruction, DOT provides us with the map of tissue properties such as total hemoglobin concentration and blood oxygen saturation via absorption coefficient. Besides the image of the absorption property of the interior of the breast, DOT gives information about cellular and subcellular changes with the aid of scattering coefficient. Even though DOT is relatively low cost, non-invasive, and capable of measuring tissue hemodynamics, it has a drawback of having insufficient spatial resolution because of the nature of light when scattered in tissue. Therefore, the accuracy of the recovered optical parameters of the tissue is limited. In this thesis, the theoretical basis of diffuse optical spectroscopy and tomography is outlined. First, this thesis examines the theory of the propagation of light in tissue. Subsequently, it describes theoretical background of the image reconstruction of diffuse optical spectroscopy and tomography. Finally, the concepts of dual modality and pharmacokinetics model which play an important role in improvement of DOT are presented by using some fundamental techniques and methods.

ÖZET

DİFFÜZ OPTİK GÖRÜNTÜLEMENİN FİZİĞİ

Diffüz optik tomografi (DOT) fonksiyonel bir görüntüleme yöntemi olup özellikle meme dokusu gibi kalın dokuları karakterize etmek için kullanılır. DOT doku özelliklerinin haritasını soğurma katsayısı aracılığıyla sağlar; örneğin toplam hemoglobin yoğunluğu ve kandaki oksijen yoğunluğu. Memenin iç bölgesinin soğurma özelliğini görüntülemesinin yanı sıra, DOT memenin hücresel ve hücre içi değişiklikleri hakkındaki bilgiyi saçılma katsayısı yardımıyla verir. DOT ucuz, zararsız ve doku hemodinamik ölçüm yapma kabiliyetine sahip olmasına rağmen ışığın dokuda saçılırken doğası gereği düşük konumsal çözünürlüğe sahip oluşu DOT için dez avantajdır. Bu yüzden, dokunun optik özelliklerinin belirlenmesi kısıtlanmış olur. Bu tezde diffüz optik spektroskopy ve tomografinin görüntüleme tekniği ve teorisi incelenmiştir. Son olarak, diffüz optik tomografinin gelişiminde önemli rol oynayan ikili yöntem ve farmakokinetik modelleme kavramları bazı önemli teknik ve metodlarla birlikte sunulmuştur.

TABLE OF CONTENTS

LIST OF FIGURES

LIST OF SYMBOLS

μ_a	Absorption Coefficient
μ_s	Scattering Coefficient

LIST OF ACRONYMS/ABBREVIATIONS

BEM	Boundary Element Method
CCD	Charged-Couple Device
CT	Computed Tomography
DOS	Diffuse Optical Spectroscopy
DOT	Diffuse Optical Tomography
EES	Extracellular Extravascular Space
FDA	Food and Drug Administration
FDM	Finite Difference Method
FEM	Finite Element Method
FVM	Finite Volume Element
ICG	Indocyanine Green
MRI	Magnetic Resonance Imaging
MONSTIR	Multichannel Optoelectronic Near infrared System for Time Resolved Image Reconstruction
NIR	Near Infared
NIRFAST	Near Infrared Fluorescence and Spectral Tomography
PET	Positron Emission Tomography
PMT	Photomultiplier tubes
RF	Radiofrequency
X-ray CT	X-ray ComputedTomography

1. INTRODUCTION

Over the past decade, optical imaging has been promising a new addition to medical imaging. Interest in optical imaging has risen in recent years compared with other imaging techniques such as MRI, CT, PET because it has several advantages. One of the most important advantages of near infrared light is its non-ionizing contrast mechanism. Another important advantage of NIR is that NIR light is low cost and it provides the functional information. Among the optical imaging modalities, diffuse optical spectroscopy and tomography originating transillumination are the new techniques to estimate functional information of thick tissue components. The underlying difference between DOS and DOT is that DOS is poor in terms of spatial location so that it enables us to obtain large spectral bandwidth whereas DOT is rich with respect to spatial location, which results in a low spectral bandwidth.

Taking background of optical imaging into consideration, in 1929, Cutler employed light to detect tumors in thick tissue. His aim was to distinguish between solid and cyst in the breast tissue. However, he obtained a blurred image due to the multiple scattering [1]. After this event, F. Jobsis discovered that it was possible to monitor the oxygenation of the brain through the skull with near infrared spectroscopy in 1977. Additionally, F. Jobsis measured value of cytochrome. Near infrared (NIR) spectroscopy was first introduced in this study [2]. Subsequently, the field of diffuse optical imaging has been developed with the help of advanced technology. In this regard, diffuse optical tomography that uses arrays of sources and detectors has been the new imaging modality providing a map of the optical properties of the medium.

DOT provides a map of tissue by using arrays of source and detectors. it suffers from poor resolution because of the diffusive nature of light propagation in tissue. In recent years, theoretical and experimental studies in DOT have been improved in order to obtain high spatial resolution and high sensitivity. Diffuse optical tomographic reconstruction using multifrequency data, dynamic contrast-enhanced diffuse optical tomography and a multimodal contrast agent for simultaneous magnetic resonance

and optical imaging of small animals have become underlying research, which we will discuss in this thesis.

1.1. The Role of Physics in Medical Imaging

The majority of the common existing biomedical imaging modalities were emerged from fundamental physics activities in the past such as the early developments of X-ray CT, the working principle of MRI, and development of PET. To illustrate, beginning with the discovery of X-ray in 1985 by Wilhem Roentgen, he played a crucial role in understanding of how radiation interacts with matter and living systems. Wilhelm Roentgen's discoveries led to the development of diagnosis radiology, radiotherapy, and nuclear medicine.

The intervention of physics in the field of medicine has led to remarkable advances in the field of medical imaging. In essence, understanding of physics of light matter has developed image processing techniques and image analysis methods, which will be discussed in the following chapters. As a result, we can expect that much of the research in physics has an important role in the development of imaging approaches for future diagnosis modalities.

1.1.1. The Principal Physics of Light Tissue Interaction

Light and matter interaction is explained by various phenomena based on atomic and molecular physics.

When an electron absorbs a photon, it may move into a state of higher energy level if the energy of the photon is higher than the energy difference between the states called as excited states. If the atom is in an excited state, it may spontaneously decay into a lower energy level by emitting a photon in a random direction. This process is also called as spontaneous emission. Furthermore, the emitted photon can go into same direction as incoming photon which is called as stimulated emission. In other words, incoming radiation is amplified. There also are two other processes, which are

florescence and phosphorescence, can be defined by regarding emission of light from chemical substance like dye molecule. There are some significant differences between florescence and phosphorescence. Phosphorescence has the capability of glowing after the excitation energy source is removed. In other words, phosphorescence has a long lifetime. Additionally, the energy released in florescence process is higher than that of phosphoresce. The amount of absorbed energy is released at the same value as the florescence energy whereas released energy is lower than absorbed energy in phosphorescence process.

Another main phenomena of the light matter interaction is scattering. There are two types of photon scattering which are elastic and inelastic scattering. Briefly, the energy of the scattered photon is the same as incident photon in elastic scattering like Rayleight and Mie scattering whereas the energy of the scattered photon is low or higher than incident photon in the inelastic scattering like Raman scattering. The later results from the movement of scattering particles [3].

1.1.2. Absorption of Light By Biological Tissue

Atoms and molecules start to collide each other. The losts of energy turns into heat within the tissue. This event is called as absorption. Absorption law is also called as Lambert's law, Lambert-Beer's law or Bouguer's law.

The transmission of light in a body was described by Bouger in 1729. In 1760, Lambert derived a mathematical form of the absorption law. Then, Lambert- Bouger law was presented according to relationship between successive layer of the sample and differential layer with thickness the fraction of incident intensity, (see Figure 1.1).

$$\frac{dI}{I} = \mu_a dx. \tag{1.1}$$

The Equation 1.1 expresses that the relationship between absorption of radiation and thickness of the medium. Here, absorption coefficient μ_a in units of inverse length (mm^{-1}) and the reciprocal of absorption coefficient $(\mu_a)^{-1}$ are defined as the probability

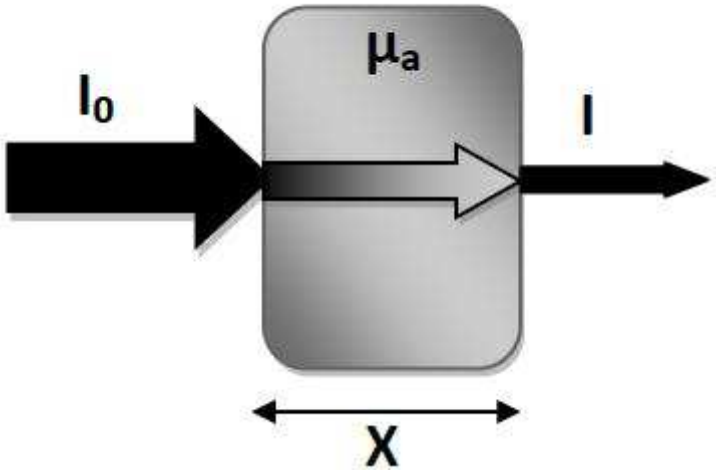

Figure 1.1. Attenuation of light through a non-scattering medium.

of a photon absorbed by the tissue per unit length, and the mean free path, respectively.

Lambert-Bouger law can also be written by the following equation

$$I = I_0 \exp(-\mu_a x). \tag{1.2}$$

In 1852, Beer stated that the absorption coefficient of compound is related to its concentration [4]

$$\mu_a = \epsilon c \tag{1.3}$$

where ϵ and c stand for the molar absorption spectra of tissue's absorption spectra (the specific absorption coefficient) and the concentration of these chromophores, respectively.

Due to the fact that polychromatic light causes a non linear relationship between concentration and absorbance, Beer-Lambert's law is valid for monochromatic light

and small concentrations. There are some important tissue chromophores which cause absorption. We will discuss absorption spectra of chromophores and find concentration of these chromophores by utilizing spectroscopic method.

1.1.3. Light Scattering in Biological Tissue

We will focus on elastic scattering of light in the medium considering that biological tissue is heterogenous. Basically, scattering results from microscopic refractive index changes which depend on the number of molecules per unit volume and polarisability. Interaction between photon and molecules in biological tissue causes photon to move in a different direction.

Scattering can be classified into two categories; namely, single and multiple scattering. According to the single scattering, the total scattered wave due to all particles is small compered with the incident wave since the separation of particle is large. The biological tissues such as cell membranes and organelles are heterogenous at microscopic scale. The reason why photons can be scattered many times before being absorbed or reemitted from the tissue is multiple scattering. When the elastic scattering is considered, there are two types of scattering which are Rayleight and Mie scattering. Rayleight scattering has same forward and backward scattered intensities. Mie scattering occurs in the forward direction. Some researchers such as Wilson and Adam (1983), Jacques *et al.* (1987) and Parsa *et al.* (1989) observed that photons in the biological region are scattered in the forward direction. Therefore, scattering in biological tissue can be explained by Mie scattering. Indeed, wavelength dependence is significant in biological tissue. However, this condition can not be predicted by Mie scattering [5]. Furthermore, we know that multiple scattering can not be ignored in biological tissue. Because new direction of scattered photons can not occur with the equal probability, we define a differential scattering coefficient

$$\mu_s = \int_{4\pi} d\mu_s(\hat{s}, \hat{s}')d\hat{s}'. \tag{1.4}$$

In this case, we can discuss the probability function of a photon to be scattered by

an angle, in other words, the phase function that a photon traveling in direction is scattered within the unit solid angle around the direction s'. In Figure 1.2, θ is angle relating the incoming photon to the scattered photon. By using these definitions, we can write the following equation;

$$p(\hat{s}, \hat{s}') = \frac{1}{\mu_s} d\mu_s(\hat{s}, \hat{s}') \tag{1.5}$$

such that $\int_{4\pi} p(\hat{s}, \hat{s}') = 1$. Due to the multiple scattering, the scattering function is characterized by an asymmetry factor g which is given by

$$g = \int_{4\pi} p(\theta) \cos\theta ds'. \tag{1.6}$$

The dimensionless asymmetry or anisotropy factor is defined as a measure of the amount of forward direction.

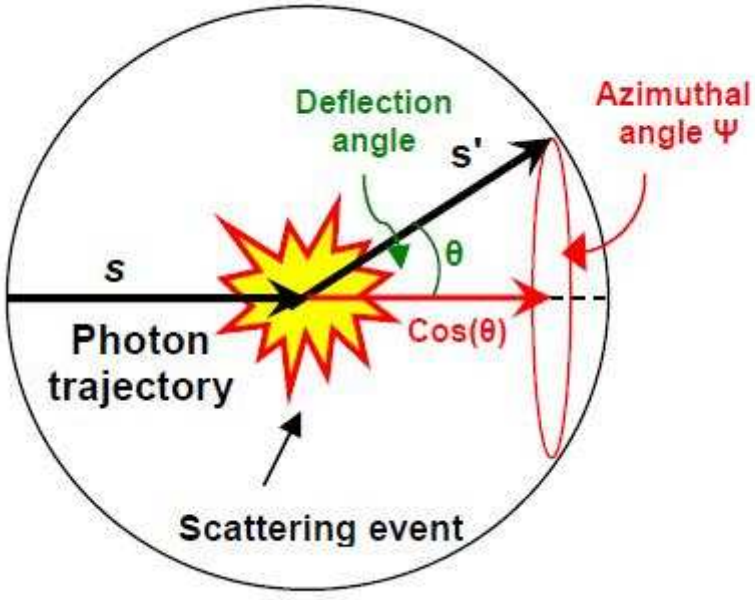

Figure 1.2. Scattering event.

We can indicate some special cases for the values of anisotropy;

$$g = 1, 0, -1 \tag{1.7}$$

correspond to purely forward scattering, isotropic scattering and purely backward scattering, respectively. In biological tissue, the anisotropy factor varies between about 0.69 and 0.99 [6]. Anisotropy factor changes with the size, shape and refractive index mismatches of the scatterers. Another fundamental description of scattering coefficient μ_s is the cross sectional area per unit volume of a medium, $\mu_s = \rho_s \sigma_s$ where ρ is the particle number density in the medium.

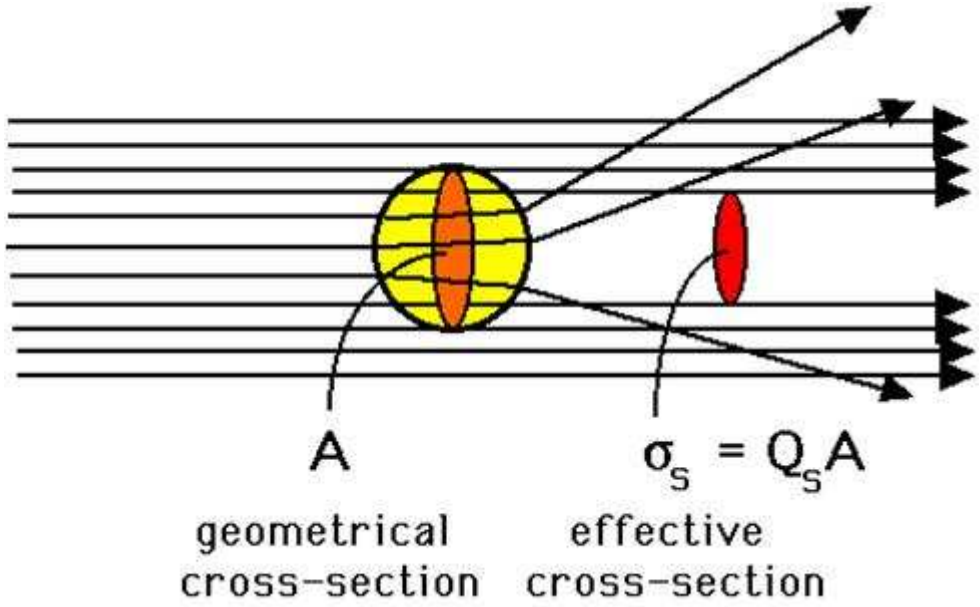

Figure 1.3. Geometrical and effective cross sectional.

By looking at the Figure 1.3, we can mention about the effective cross section that is the size of scattering shadow. Here, $\sigma_s = Q_s A_s$ where Q_s is the scattering efficiency.

In the biological tissue, both absorption and scattering take place so this type of

media is called as a turbid media. Therefore, total attenuation can be described as

$$\mu_t = \mu_a + \mu_s. \tag{1.8}$$

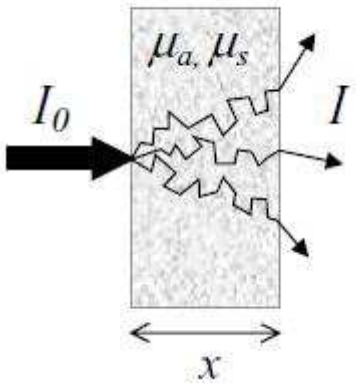

Figure 1.4. Attenuation of light through a scattering medium [7].

In the case of single scattering, the transmitted intensity is given by

$$I = I_0 exp(-\mu_t x) \tag{1.9}$$

where I_0 stands for incident intensity of the light in turbid medium. Additionally, μ_t represents the total attenuation coefficient, $\mu_t = \mu_a + \mu_s$. In here, combining the scattering coefficient and the anisotropy factor gives a feasible equation such that $\mu_{s'} = (1-g)\mu_s$ where $\mu_{s'}$ is a reduced (transport) scattering coefficient resulting from incorporation scattering coefficient and anisotropy factor. Then, we can write a transport interaction coefficient, which is $\mu_{t'} = \mu_a + \mu_{s'}$. The reciprocal of $\mu_{t'}$ is referred as the transport mean free path. With the aid of these pivotal definitions mentioned above, we will discuss radiative transport equation in Chapter 2.

1.2. Diffuse Optical Spectroscopy and Tomography

In order to understand how spectroscopy monitors functional information of tissue, it is necessary to use some significant concepts about optical properties of tissue mentioned previously. The propagation of laser light in tissue depends on constitutions of biological tissue such as hemoglobin, water, and lipid. Even though biological tissue behaves as diffusive media in optical window, functional information is obtained by the absorption of chormophores like oxy-deoxy hemoglobin. For example; the concentration of oxy and deoxy hemoglobin provides demonstration how well oxygenated the blood is. A measure of the oxygenation of blood can be given as $SO_2 = \frac{[HbO_2]}{[HbO_2+Hb]}$ where SO_2, $[HbO_2]$ and $[Hb]$ represent the oxygen saturation, the concentration of oxy-haemoglobin, and deoxy-haemoglobin, respectively. By using spectroscopy, we can measure the absorption spectra of oxy-deoxy hemoglobin.

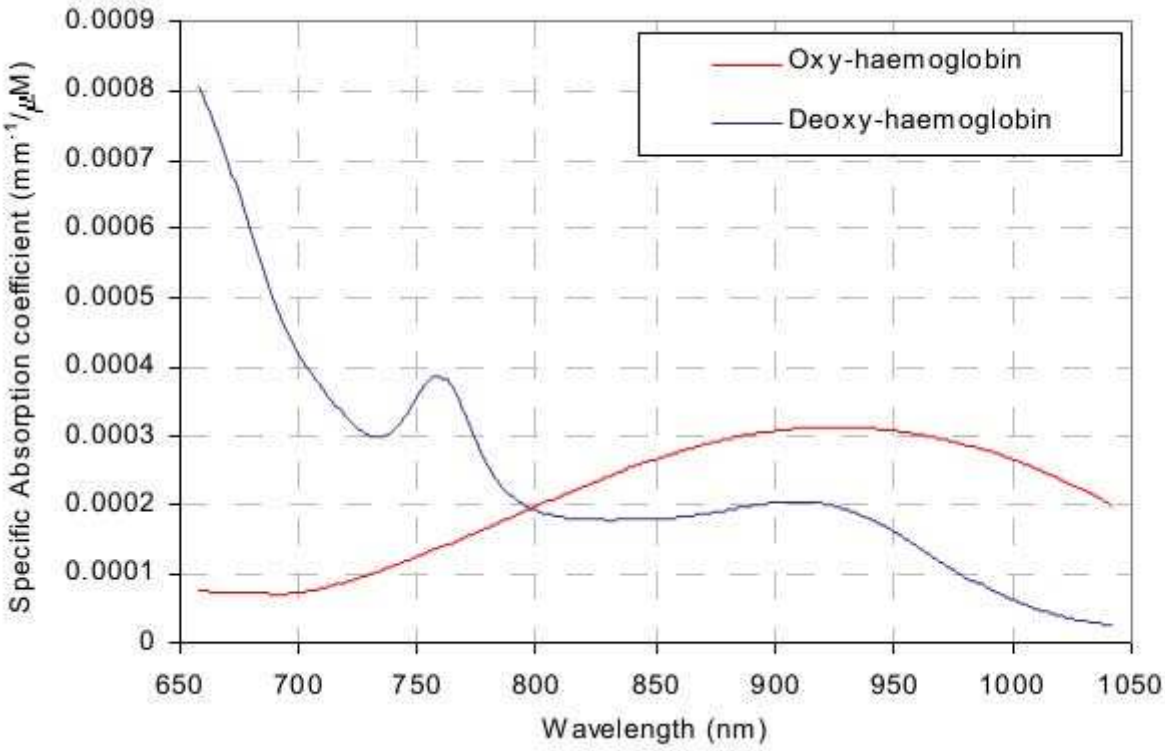

Figure 1.5. The absorption spectra of oxy and deoxy- haemoglobin in the near infrared wavelength range [7].

In this case, we know absorption coefficients and extinction coefficients at two

wavelength, so we can construct specific model by using Beer-Lambert Law.

$$\mu_{780nm} = \varepsilon_{HbO_2}(780nm)C_{HbO_2} + \varepsilon_{Hb}(780nm)C_{Hb} \tag{1.10}$$

and

$$\mu_{820nm} = \varepsilon_{HbO_2}(820nm)C_{HbO_2} + \varepsilon_{Hb}(820nm)C_{Hb}. \tag{1.11}$$

Two unknowns and two equations can provide us with calculation of oxygen saturation ($S0_2$).

$$SO_2 = \frac{\varepsilon_{Hb1}\mu(820) - \varepsilon_{Hb2}\mu(780)}{(\varepsilon_{Hb1}\mu(820) - \varepsilon_{Hb2}\mu(780)) + (\varepsilon_{HbO_2}(820)\mu(780) - \varepsilon_{Hb1}\mu(820))} \tag{1.12}$$

where $\varepsilon_{Hb1} = \varepsilon_{Hb}(780nm)$ and $\varepsilon_{Hb2} = \varepsilon_{Hb}(820nm)$ [7].

After describing diffuse optical spectroscopy, we can express diffuse optical tomography regarding tissue optical properties for many volume elements within tissue region. Topographic (2D, surface mapping) imaging and tomographic imaging (3D, volume measurements) have similar formalism so we can call tomography which refers to both of them. Considering tomography, we remind X-ray computed tomography scanner (CT) and its traditional methods. In the early 1970's, X-ray computed tomography scanner was introduced by Hounsfield. Imaging method of CT acquires data over a series of projection angles. This projection data is used in order to form a cross sectional image. Even though X-rays scatter in tissue (a random phenomenon), we can assume that the photons travel in straight lines because scattering photons can be ignored compared with the photons which pass through straightly. In this case, we can use feasible algorithms like Radon transform in order to obtain image reconstruc-

tion [8]. When we use cross sectional image reconstruction for near infrared optical tomography, we obtain a detrimental image because near infared light can not travel straight line in soft tissue. Near infared light attenuates according to absorption and scattering properties of tissue. Understanding the propagation of light in tissue plays an important role in image reconstruction for DOT. Researchers have used the mathematical model of transport theory which we will discuss in the flowing chapter to reconstruct image for diffuse optical tomography.

1.3. Clinical Application of Diffuse Optical Spectroscopy and Tomography

Optical imaging has several clinical applications. In the literature, three main applications are in breast cancer diagnosis and characterization, functional brain imaging, and imaging skeletal muscle. Optical Imaging has been preferred to use in clinical application instead of other imaging modalities in recent years because they have some subtle drawbacks. For instance, mammography does not work well in dense breasts. MRI and mammography have high sensitivity, and low specificity. Therefore, a patient may be exposed to unnecessary biopsies. Furthermore, position emission tomography provides the metabolic function in tissue but it requires the injection of exogenous radionuclides. Compared with these modalities, NIR diffuse optical spectroscopy and tomography are essential in the detection of breast cancer. Thus, the majority of patients can get rid of unnecessary biopsies. Application of DOS and DOT helps researchers to obtain information about characterization of breast tissue.

According to cancer research, hemoglobin concentration is the basic factor for distinguishing between benign and malignant tumor. Hemoglobin concentration increases owing to the angiogenesis that is the growth of new blood vessel in cancerous tissue owing to the tumor growth. Furthermore, tissue hypoxia is found in malignant tumor [9].

In the literature, there are crucial articles on the estimation of hemoglobin and water concentration, oxygen saturation, and scattering estimates for healthy female breast tissue and breast tumors. To illustrate, an increase in the blood volume is

observed at the location of cancerous tumors so this increase has been estimated to correspond to a two to four fold increase in hemoglobin concentration within breast cancer tumors relative to healthy tissue [10, 11]. At the same time, a localized 1.4 to 4.4 decrease in oxygen partial pressure is present within breast cancers [9]. These two physiological factors characterize suspicious mammographic abnormalities. The other significant factor is a scattering coefficient. Scattering spectra changes due to the size, distribution, volume fraction of the particles, and refractive index [12]. The aforementioned theory -Mie theory- can be simplified according to the scattering spectra. Thus, scattering amplitude and scattering power images can be obtained reasonably by applying a simpler approximation to Mie Thory. While the amplitude images give information about the number of density of the scatters, scatter power images are obtained from the knowledge about average scatter size. When we consider that the hallmark of an epithelial malignancy is an increase in the overall epithelial cell density with increased nuclear and nucleolar size, we can indicate that benign and malignant tumors have different cellular and organelle density, and size. There are various important studies that include scattering contrast between malignant and benign tumors [13]. Although microscopic sub-cellular alterations can not be detected in the pathological analysis, scattering coefficient obtaining from DOT provides psychological information about molecular level changes. In this case, we can indicate that DOT plays an important role in distinguishing between benign and malignant tumors. Actually, NIR imaging techniques in breast cancer not only help to detect tumor but also yield the early identification of treatment response in patients undergoing neoadjuvant therapy.

Another application of DOI is the brain imaging as far back as 1977 [2]. Because diffuse optical imaging has the capability of monitoring brain activation in vivo, researchers have aimed at understanding how the brain functions. One of the purposes of the applying to diffuse optical imaging is obtaining knowledge about brain functions. Another aim of DOI brain imaging is to diagnose and monitor the diseases such as stroke, epilepsy, and brain injury. The systems such as CW, frequency domain, time domain for brain application DOI have been improved. In the literature, there are some researches about brain applications for DOI. To illustrate, 32-channel time resolved optical imaging system developed by the group at University College London has

been successful to image the brain of premature infant with a cerebral hemorrhage [14]. The skull of infant is soft and thinner than adult head so that premature infants are suitable for transillumination measurements.

On the other hand, some researchers have presented existence of void regions to obtain tomographic images of neonatal head [15]. Therefore, we can indicate that brain applications for DOI do not play an important role in medical imaging as breast applications mentioned above. In this thesis, we will prefer to focus on explaining techniques for DOS and DOT in breast cancer detection.

1.4. Advances in DOT

After the discovery of the ability to measure oxygen saturation changes of the blood through the cat cranium, this method has been widespread. Near infared optical measurements yield functional information about tissue blood content and oxygenation. These measurements also provide information about tissue structure due to scattering spectrum. However, spatial resolution is poor due to the fact that scattering is multiple in biological tissue. In order to enhance spatial resolution, researchers have attempted to improve NIR imaging capabilities in terms of instrumentation, modeling, and image reconstruction. In 1997, two reviews of optical imaging in medicine became indispensable parts of DOT. One of them which summarized instrumentation and experimental techniques was published by Hebden [16]. The other one includes theoretical approaches to image reconstruction [17]. In this view, we can divide into two categories.

1.4.1. The Development of Instrumentation for DOT

The use of advanced source and detection technology enabled us to improve intensity attenuation measurements after developing of diffuse optical spectroscopy at the end of the 1980's. After Hounsfield was awarded the 1979 Nobel Prize for medicine, researchers have started to comprehend and developed the techniques of X-ray CT.

Indeed, diffuse optical spectroscopy is an integral part of DOT. Tomographic techniques combine photon trajectories at different angles and yield three dimensional distribution of optical tomography. In DOT system, we have source and detectors which are placed around the object to be imaged. The usage of different sources and detectors contributes to data collection.

Firstly, we may concentrate on types of DOT. There are three common types; continuous wave,intensity modulated, time domain. In the continuous wave mode, the signal provides fast data acquisition but do not have the capability of separating absorption from scattering coefficient in bulk medium. In other words, obtaining the intensity of light does not does not enable us to distinguish between effects of scattering and absorption. Frequency domain technique gives more information about the medium than direct current system. This system for tissue measurements was defined by Duncan *et al.* in 1993. Subsequently, Poque *et al.* introduced frequency domain optical tomography system in 1997. Since then, researchers have followed the development of frequency domain optical tomography and published hundreds of articles. In the frequency domain system, there are phase and amplitude differences between transmitted and original signals. This system gives discrete information about absorption and scattering coefficients. Additionally, the time domain system is the richest in terms of acquiring information. However, it is slowest in data acquisition and the most expensive among the three modes. This technique is significant in terms of distinguishing from scattering and absorption effects. By this technique, we can get information on the increased pathlength of light in medium owing to multiple scattering events. The length of path gives the absorption effect. To illustrate, a region in which absorption is higher causes the pulse to narrow. Conversely, a region in which scatter is higher causes the pulse to broaden so photons have traveled further.

The use of time-domain measurement was started by Chance *et al.* [18]. The recovery of optical properties from time resolved measurements was actualized by analytical solutions presented by Patterson *et al.* [19]. In 1991, Fishkin *et al.* and Patterson *et al.* stated analytical solutions in order to compare with measurements from frequency domain system [20, 21].

Secondly, the advances in the field of fiber optics, laser, and detectors for DOT have played an important role in constructing NIR data acquisition system. After development of first laser in 1960 by Theodore Maiman, semiconductor lasers have exploited. These types of lasers are inexpensive and stable so we can use them in CW and frequency domain systems. Another important type of lasers for DOT systems which occurred in the 1970s is mode-locked laser. These lasers are pulsed lasers and more sensitive to motion. Detectors for DOT system are the key to collect better NIR data acquisition. Generally, photomultiplier tubes, charged couple devices and photodiodes are common detectors. Especially, PMTs were widespread in the late 1930s. Later, CCD and PD (solid state detectors) which have a large dynamic range and stable at low frequency were developed. In contrast to CCD, PMT detectors are sensitive at high frequency, and have a large detection area [22].

1.4.2. The Development of Theoretical Models for DOT

In the past, light transport in tissue was modeled with many approaches consisting of Maxwell's equations. However, the mostly unknown dielectric properties of tissue components make it impossible to apply Maxwell equations. Ishimaru presented two significant theories in 1978. One of them is multiple-scattering theory which is based on Maxwell's equations [23]. The other is Radiative transfer equation, which will be discussed in Chapter 2.

Researchers proved that solution to multiple scattering theory is highly complex. However, this mathematical modeling in tissue was not enhanced for optical tomography. As a result of this, the light transport theory in tissue was generated as a new field of study, the photon migration. Thanks to advances in the field of photon migration, the Radiative transfer equation was approximated to the diffusion equation. Subsequently, diffusion approximation contributes to obtain a feasible mathematical basis for tomographic image reconstruction. Singer *et al.* introduced a model-based image reconstruction method based on diffuse radiation [24]. Furthermore, Arridge used finite element method for light propagation in tissue based on time resolved diffusion approximation [25, 26].

It can be said that the majority of studies on NIR spectroscopy and tomography were published in 1990s. TOAST (time-resolved optical absorption and scatter tomography) became the first algorithm which was developed using FEM and diffusion approximation [27]. Subsequently, MONSTIR (multi-channel opto-electronic near infra-red system for time-resolved image reconstruction) project began in 1996. The MONSTIR instrument was used in the University College Hospital neonatal intensive care to obtain data on two premature babies. This system consists of 32 fibre bundles providing image data set by using the measurements of 1024 the temporal point spread function [28]. The other group at Darmouth College obtained quantitative images from multiple-wavelength frequency domain measurements with a circularly symmetric imaging geometry. McBride *et al.* reported these quantitative images of hemoglobin concentration and oxygen saturation in tissue-like phantoms containing oxygenated and de-oxygenated blood in a highly scattering medium [22]. In order to implement computational finite element model of the diffuse approximation to model light propagation, Dehghani *et al.* constructed a toolbox (NIRFAST) in matlab (matrix laboratory) [29].

Unfortunately, we can not get rid of the undesirable properties of DOT such as its ill-posedness and non-uniqueness with the help of advances in modeling and reconstruction techniques. In other words, spatial resolution of diffuse optical imaging is restricted by the high degree of scattering. In order to enhance spatial resolution, researchers have used additional information from other imaging modalities such as X-ray CT, ultrasound, and MRI. The most popular and feasible trend of multi-modality imaging system which was developed at Dartmouth College is the combined DOT and MRI. The majority of researchers obtained priori information about the location and the size of the tumor utilizing MRI in order to reduce unknown parameters for image reconstruction. In general, this information is called priori information. Some fundamental studies demonstrated that priori information manifests the quantitative accuracy of absorption and scattering of tumors [30–32].

Other improvement process of DOT is the usage of exogenous contrast agents. With the help of exogenous contrast dyes, we can differentiate between malignant and

benign tumors because healthy and diseased tissues have different hemoglobin contents. The most common endogenous contrast is indocyanine green (ICG) which is suitable for DOT. It is approved by the Food and Drug Administration (FDA) and has been used in the medical field since 1956. Some studies demonstrated that ICG has different effects on benign and malignant tumors. Therefore, we can say that ICG enhances absorption of human breast cancer in vivo [33–35]. Another advantage of applying contrast agent for DOT is the development of bi-functional imaging probes. It is a fact that each of imaging mobilities has different set of parameters. When bi-functional contrast agent is used, good tumor localization and similar contrast agent kinetics are obtained [36]. Furthermore, ICG has not only absorption spectra but also fluorescence spectra in the near infrared region. By using fluorescence signal from ICG, researchers get an additional information about tissue micro environment such as pO_2, pH, and intracellular calcium concentration [37, 38].

2. LIGHT TRANSPORT IN TISSUE

The propagation of light in biological tissue results in multiple scattering process. As it was discussed in the previous chapter, Ishimaru developed multiple scattering theory which is based on Maxwell equations in order to model a multiple scattering problem. This model is not feasible because the electromagnetic theory which preserves the wave properties of light includes complexity of mathematical formalism. Instead of this model, the transport theory based on conservation of the energy is much simpler and more efficient mathematical model in order to describe a photon migration in biological tissue [39]. We can discuss some significant differences and similarities between these two theories. The electromagnetic theory concerns with superposition of electromagnetic fields, in other words the properties of light such as polarization, interference are considered in this theory while transport theory depends on superposition of energy flux. On the other hand, we can indicate that poynting vector which refers the energy transport of electromagnetic waves may be compared with the flux vector in transport theory. There is the similarity between electromagnetic and transport theory with respect to radiant power (P) transferred through a surface with the area (A).

$$P = \int_A \mathbf{S}\,\mathbf{n}\,dA \tag{2.1}$$

for electromagnetic theory; where S is poynting vector

$$P = \int_A \mathbf{S}\,\mathbf{n}\,dA \tag{2.2}$$

for transport theory; where **F** is the flux vector.

In this chapter, we will express the Radiation transfer equation and it will be simplified in the diffusion approximation. After obtaining diffusion equation, we can suggest some analytical solutions in the presence of boundaries. Although analytical solutions are fast and give accurate values, these solutions only exist for homoge-

nous objects. Therefore, the diffusion equation is solved by numerical methods. Even though Monte Carlo is the most common method among numerical solutions, it has drawback of time-consuming. All of these suggestions are considered, the most appropriate method to solve the diffusion equation and model an image reconstruction for inhomogeneous object is finite element method.

2.1. The Derivation of The Radiative Transfer Equation

Before we describe linear transport equation, it is essential to explain some fundamental optical parameters such as the propagation of photons, the radiance, fluence rate, and flux [39].

2.1.1. Photon Distribution Function and Photon Power

The power of photons that travels through the infinitesimal is dS in the infinitesimal solid angle $d\Omega$ in the direction of s, with velocity $c_t = \frac{c_0}{n}$, and energy $\hbar\nu$ is defined as

$$dp = N(\mathbf{r}, \hat{s}) dS d\Omega c_t \hbar\nu \tag{2.3}$$

where $N(\mathbf{r}, s)$ is the photon distribution function, which is referred to as the number of photons per unit volume traveling in the direction of unit vector $\hat{s}$, in an element of solid angle containing $\hat{s}$, divided by that element, at a given point r.

2.1.2. Radiance

In order to describe the propagation of the photon power with a specific direction $\hat{s}$, through small surface dS, we can use the quantity that is radiance.

$$L(\mathbf{r}, \hat{s}) = \frac{dp(\mathbf{r}, \hat{s})}{dS d\Omega} \tag{2.4}$$

Furthermore, with the aid of Equation 2.3, we can defined as

$$L(\mathbf{r}, \hat{s}) = N(\mathbf{r}, \hat{s})\frac{hc^2}{\lambda} \tag{2.5}$$

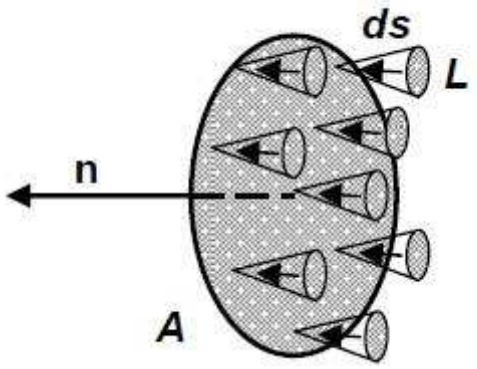

Figure 2.1. The radiance [39].

2.1.3. Fluence Rate

The fluence rate can be expressed as the energy flow per unit area irrespective to the flow direction, Figure 2.2.

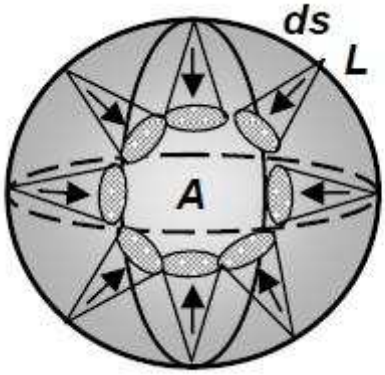

Figure 2.2. The fluence rate [39].

In other words, fluence rate (intensity) is the integral of the radiance over all

direction

$$\Phi(\mathbf{r},\mathbf{t}) = \int_{4\pi} L(\mathbf{r}, \hat{s}, t) d\Omega. \tag{2.6}$$

2.1.4. Net Flux

The other useful quantity is the net energy flow per unit area, which is called the flux. We can define as

$$F(\mathbf{r}) = \int_{4\pi} L(\mathbf{r}, \hat{s}) \hat{s} d\Omega, \tag{2.7}$$

which represents the amount of the net flux of power regardless of the direction of that. In order to comprehend the difference between the terms of fluence rate and flux, we

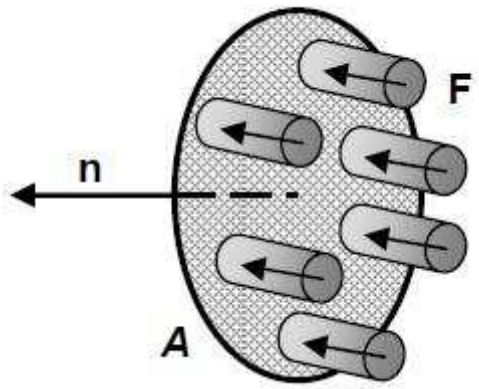

Figure 2.3. The flux [39].

may express the relationship between these terms in the following equation;

$$F(\mathbf{r}) = \int_{-\infty}^{\infty} \Phi(\mathbf{r}, t) dt. \quad \frac{J}{m^2} \tag{2.8}$$

Thanks to these quantities mentioned above, we can derive the RTE transfer equation by applying principles of the conservation of energy. In this case, we consider

that photons travel at speed c in direction $\hat{s}$ within a small volume dV. According to the conservation of energy, the addition and the substraction of photons from photon distribution function in specific interaction should be taken into consideration.

Firstly, we can define the first term of the transport equation representing the change of the photon distributions a function of time, (see Figure 2.4).

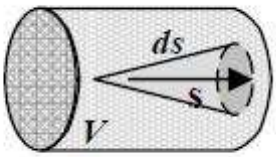

Figure 2.4. The energy of the photons in volume [39].

$$\int \frac{\partial N(\mathbf{r}, \hat{s}, t)}{\partial t} dV. \tag{2.9}$$

The second term of the transport equation indicates the photon lost through the boundary, (see Figure 2.5).

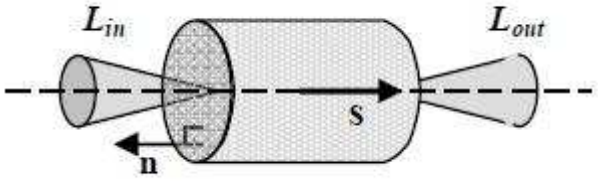

Figure 2.5. Losses through the boundary [39].

$$-\oint_s cN(\mathbf{r}, \hat{s}, t)\hat{s}dS. \tag{2.10}$$

Additionally, this term can be expressed such that $-\int_v c\nabla N(\mathbf{r}, \hat{s}, t)dV$ by using Gauss' theorem. The third therm represents absorption of incoming photons in the direction

$\hat{s}$, Figure 2.6.

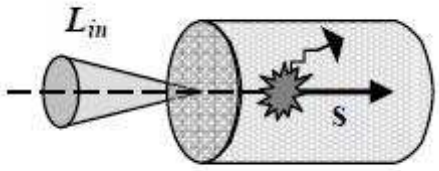

Figure 2.6. Losses due to the absorption [39].

$$-\int_V c\mu_a N(\mathbf{r},\hat{s},t)dV. \tag{2.11}$$

Another important term consists of the photons scattering from direction $\hat{s}$ into any other direction $\hat{s}'$, by looking at the Figure 2.7.

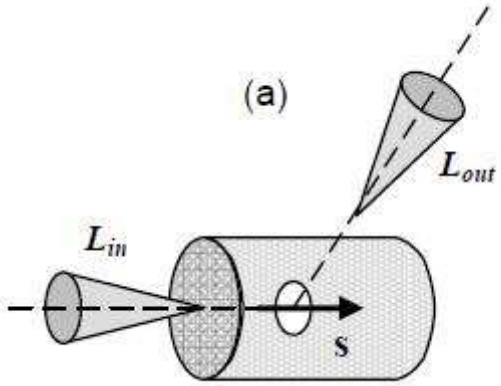

Figure 2.7. Losses due to the scattering [39].

$$-\int_V c\mu_s N(\mathbf{r},\hat{s},t)dV \tag{2.12}$$

The fifth term represents the photons gained through scattering from any direction $\hat{s}'$ into the direction $\hat{s}$, Figure 2.8.

$$+\int_v c\mu_s(r)\int_{4\pi} P(\hat{s},\hat{s}')N(\mathbf{r},\hat{s}',t)dS'dV. \tag{2.13}$$

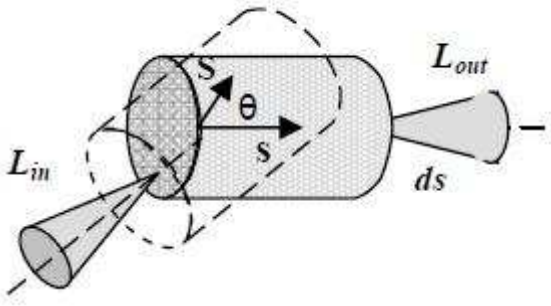

Figure 2.8. The gain through scattering from any direction to direction $\hat{s}$ [39].

The last term yields the photons gained through a light source, "q", Figure 2.9.

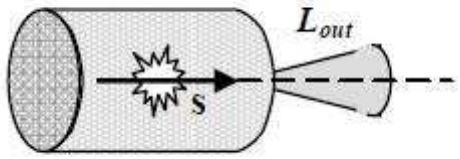

Figure 2.9. The gain due to the a light source within volume V [39].

$$\int_V q(\mathbf{r}, \hat{s}, t) dV. \tag{2.14}$$

As a result of constructing these terms mentioned above, we access time-dependent the Radiation transfer equation.

$$\int \frac{\partial N(\mathbf{r}, \hat{s}, t)}{\partial t} dV = -\int_v c\nabla N(\mathbf{r}, \hat{s}, t) dV - \int_V c\mu_a N(\mathbf{r}, \hat{s}, t) dV - \int_V c\mu_s N(\mathbf{r}, \hat{s}, t) dV + \int_v c\mu_s(r) \int_{4\pi} N(\mathbf{r}, \hat{s}', t) d\hat{s}' dV + \int_V S(\mathbf{r}, \hat{s}, t). \tag{2.15}$$

Here, note that $ds^{'}$ was used instead of $d\Omega$.

Furthermore, we can express Equation 2.15, in terms of radiance by using Equa-

tion 2.4;

$$\frac{1}{c}\frac{\partial L(\mathbf{r},\hat{s},t)}{\partial t} + \hat{s}\nabla L(\mathbf{r},\hat{s},t) + (\mu_a+\mu_s)L(\mathbf{r},\hat{s},t) = \mu_s \int L(\mathbf{r},\hat{s},t)p(\hat{s}',\hat{s})d\hat{s}' + S(\mathbf{r},\hat{s},t). \tag{2.16}$$

Although there are some analytical solutions to RTE in the literature [40], these solutions are not feasible. Additionally, some numerical solutions of RTE such as Monte Carlo method are available. On one hand, this method has accurate and an adaptable solution, on the other hand, it is computationally intensive and time consuming because the radiance is highly anisotropic in biological tissue [41]. The best way to tackle RTE is applying to an approximate solution that is the diffusion equation.

2.2. The Diffusion Approximation to the RTE

Diffusion theory expresses the propagation of light in the strong scattering regime. It is much simpler and more useful than RTE. Derivation of diffusion equation was published by several authors [42, 43]. Diffuse approximation is given by Equation 2.17 [43].

$$\frac{\partial \Phi(\mathbf{r},t)}{c\partial t} + \mu_a\Phi(\mathbf{r},t) - D\nabla^2\Phi(\mathbf{r},t) = S(\mathbf{r},t) \tag{2.17}$$

where $\Phi(\mathbf{r},t)$; the photon fluence rate at position r and time t, $S(\mathbf{r},t)$; the source distribution of photons, D; the photon diffusion coefficient and μ_s; the reduced scattering coefficient, c; the speed of light in the medium, μ_a; the absorption coefficient.

This Equation 2.17 is constructed with the help of some significant assumptions. According to the diffusion approximation which is Equation 2.17, we can assume that diffuse intensity is scattered in all direction after encountering many particles, in this case, its angular distribution is almost uniform isotropic [23].

2.2.1. First Approximation

Considering that the fluence rate is isotropic, we can expand radiance with the aid of spherical harmonics. In other words, this approximation implies that the scattering is much greater than absorption.

$$L(\mathbf{r},\hat{s},t) = \frac{1}{4\pi}\Phi(\mathbf{r},t) + \frac{3}{4\pi}\mathbf{J(r,t)}\hat{s}. \tag{2.18}$$

By using this approximation for the radiance, we will be obtained two differential equations; scalar and vector differential equations.

Before applying to the first approximation into Equation 2.16, this is integrated over the 4π solid angle;

$$\int_{4\pi}\frac{1}{c}\frac{\partial L(\mathbf{r},\hat{s},t)}{\partial t}d\Omega + \int_{4\pi}\hat{s}\nabla L(\mathbf{r},\hat{s},t)d\Omega + (\mu_a+\mu_s)\int_{4\pi}L(\mathbf{r},\hat{s},t)d\Omega = \mu_s\int_{4\pi}\int L(\mathbf{r},\hat{s},t)p(\hat{s}',\hat{s})d\Omega' d\Omega + \int_{4\pi}q(\mathbf{r},\hat{s},t)d\Omega. \tag{2.19}$$

2.2.1.1. The Scalar Differential Equation. On the basis of the Equation 2.19, the left hand side can be written as $\int_{4\pi}\frac{\partial L(\mathbf{r},\hat{s},t)}{c\partial t}d\Omega = \frac{\partial\Phi(\mathbf{r},\hat{s},t)}{c\partial t}$ by using Equation 2.6.

The second term on the left hand side of the Equation 2.19 can be regulated by using vector identity. $\hat{s}\nabla L = \nabla(\hat{sL}) - L\nabla\hat{s}$. However, $\nabla\hat{s} = 0$. Then, we obtain

$$\int_{4\pi}\hat{s}\cdot\nabla L(\mathbf{r},\hat{s},t)d\Omega = \int_{4\pi}\nabla\cdot[\hat{s}L(\mathbf{r},\hat{s},t)]d\Omega = \nabla\cdot\int_{4\pi}\hat{s}L(\mathbf{r},\hat{s},t)d\Omega. \tag{2.20}$$

By using a beneficial definition such that $\mathbf{J(r,t)} = \int_{4\pi}\hat{s}L(\mathbf{r},\hat{s},t)$, we can obtain this equality, $\nabla\int_{4\pi}\hat{s}L(\mathbf{r},\hat{s},t)d\Omega = \nabla\cdot\mathbf{J(r,t)}$.

The third term on the left hand side can be simplified such that $\mu_t \int_{4\pi} L(\mathbf{r}, \hat{s}, t) d\Omega = \mu_t \Phi(\mathbf{r}, t)$ where $\mu_t = \mu_a + \mu_s$.

For the first term on the right hand side of Equation 2.19, we can use the first approximation and we obtain

$$\mu_s \int_{4\pi} [\int_{4\pi} L(\mathbf{r}, \hat{s}', t) d\Omega'] P(\hat{s}', s) d\Omega = \frac{\mu_s}{4\pi} \int_{4\pi} \int_{4\pi} [\Phi(\mathbf{r}, t) + 3\mathbf{J(r,t)} \cdot \hat{s}] P(\hat{s}', s) d\Omega' d\Omega. \tag{2.21}$$

Furthermore, we can evaluate Equation 2.21 step by step $\int_{4\pi} [\int_{4\pi} \Phi(\mathbf{r}, t) P(\hat{s}', \hat{s}) d\Omega'] d\Omega = \Phi(\mathbf{r}, t) \int_{4\pi} [\int_{4\pi} P(\hat{s}', \hat{s}) d\Omega'] d\Omega = \Phi(\mathbf{r}, t) \int_{4\pi} d\Omega = 4\pi \Phi(\mathbf{r}, t)$.

The second part of Equation 2.21;

$$\begin{aligned} &\int_{4\pi} \int_{4\pi} [\mathbf{J(r,t)} \cdot \hat{s}'] P(\hat{s}', \hat{s}) d\Omega' d\Omega \\ &= |\mathbf{J(r,t)}| \int_{4\pi} [\int_{4\pi} P(\hat{s}', \hat{s}) d\Omega] \cos\theta' d\Omega' \qquad (2.22) \\ &= |\mathbf{J(r,t)}| \int_{4\pi} \cos\theta' d\Omega' \qquad (2.23) \\ &= 0. \qquad (2.24) \end{aligned}$$

Note that $d\Omega' = sin\theta' d\theta' d\phi'$. As a result of these parts, we can obtain a simple equation such that

$$\frac{\mu_s}{4\pi} \int_{4\pi} [\int_{4\pi} L(\mathbf{r}, \hat{s'}, t) d\Omega'] d\Omega = \mu_s \Phi(\mathbf{r}, t). \tag{2.25}$$

Finally, the source term is an isotropic due to the fact that $S(\mathbf{r}, \hat{s}, t)$ does not depend on $\hat{s}$. Therefore, source term is written as $\int_{4\pi} S(\mathbf{r}, \hat{s}, t) d\Omega = \frac{1}{4\pi} \int_{4\pi} S(\mathbf{r}, t) d\Omega = S(\mathbf{r}, t)$.

These parts evaluated above construct following scalar differential equation;

$$\frac{\Phi(\mathbf{r},t)}{c\partial t} + \mu_a \Phi(,\mathbf{r},t) + \nabla \mathbf{J}(\mathbf{r},t) = S(\mathbf{r},t). \tag{2.26}$$

2.2.1.2. The Vector Differential Equation. Multiplying both sides Equation 2.16 by $\hat{s}$ and using the first approximation , we will be obtained the vector differential equation.

$$\int_{4\pi} \hat{s} \frac{\partial L(\mathbf{r},\hat{s},t)}{c\partial t} d\Omega + \int_{4\pi} \hat{s}(\hat{s}.\nabla L) d\Omega + \mu_t \int_{4\pi} \hat{s} L(\mathbf{r},\hat{s},t) d\Omega = \int_{4\pi}\int_{4\pi} \hat{s}[L(\mathbf{r},\hat{s'},t) P(\hat{s'},\hat{s}) d\Omega'] d\Omega + S(\mathbf{r},\hat{s},t). \tag{2.27}$$

For the first term on the left hand side of the Equation 2.27 can be regularized by using definition such that $\mathbf{J(\ r,t)} = \int_{4\pi} \hat{s} L(\mathbf{r},s,t) d\Omega$. We obtain;

$$\int_{4\pi} \hat{s} \frac{\partial L(\mathbf{r},\hat{s},t)}{c\partial t} d\Omega = \frac{\partial J(\mathbf{r},t)}{c\partial t}. \tag{2.28}$$

The second term on the left hand side of Equation 2.27 becomes

$$\int_{4\pi} \hat{s}(\hat{s}.\nabla L) d\Omega = \frac{1}{4\pi} \int_{4\pi} \hat{s}(\hat{s}.\nabla \Phi) d\Omega + \frac{3}{4\pi} \int_{4\pi} \hat{s}[\hat{s} \cdot \nabla(\mathbf{J} \cdot (\hat{s})] d\Omega. \tag{2.29}$$

We evaluate two integrals respectively, from Equation 2.29. For the first integral, we can write as,

$$\int_{4\pi} \hat{s}(\hat{s}.\mathbf{A})d\Omega = \int\int \hat{s}\mathbf{A}\cos\theta\sin\theta d\theta d\phi = \int_0^{2\pi}\int_0^{\pi} A(\sin^2\cos\theta\cos\phi d\theta d\phi)\hat{i} + \int_0^{2\pi}\int_0^{\pi} A(\sin^2\theta\cos\theta\sin\phi d\phi)\hat{j} + \int_0^{2\pi}\int_0^{\pi} A(\cos^2\theta\sin\theta d\theta d\phi)\hat{k} \quad (2.30)$$

where $\mathbf{A} = \nabla\Phi$ and $\mathbf{A}$ is independent of $\hat{s}$. Here, the first and second integrals are equal to zero, and the third integral is evaluated such that $\int_0^{2\pi}\int_0^{\pi} A(\cos^2\theta\sin\theta d\theta d\phi)\hat{k} = \int_0^{2\pi}\int_{-1}^{+1} u^2 du d\phi A\hat{k} = 2\pi[\frac{u^3}{3}]_{-1}^{+1}\mathbf{A} = \frac{4\pi}{3}\mathbf{A}$

We obtain that $\int_{4\pi}\hat{s}(\hat{s}.\mathbf{A})d\Omega = \frac{4\pi}{3}\mathbf{A}$.

Finally, Equation 2.29 becomes $\int_{4\pi}\hat{s}(\hat{s}.\nabla L)d\Omega = \frac{1}{3}\nabla\Phi$.

By using the definition that is $\mathbf{J}(\mathbf{r},t) = \int_{4\pi}\hat{s}L(\mathbf{r},s,t)d\Omega$, the third term on the right hand side of the Equation 2.27, $(\mu_t\int_{4\pi}\hat{s}L(\mathbf{r},\hat{s},t)d\Omega)$, can be written as $\mu_t\mathbf{J}(\mathbf{r},\hat{s},t)$. For the first term on the right hand side from Equation 2.27, we can use first approximation and make some calculation to simplify this term.

$$\int_{4\pi}\int_{4\pi}\hat{s}[L(\mathbf{r},\hat{s}',t)P(\hat{s}',\hat{s})d\Omega']d\Omega = \frac{1}{4\pi}\int_{4\pi}\int_{4\pi}\hat{s}[\Phi(\mathbf{r},t)P(\hat{s'},\hat{s})d\Omega']d\Omega + \frac{3}{4\pi}\int_{4\pi}\{\hat{s}\int_{4\pi}[\mathbf{J(r,t)}\cdot\hat{s}']P(\hat{s}',\hat{s})d\Omega'\}d\Omega. \quad (2.31)$$

These two parts of Equation 2.31 can be evaluated respectively. The first integral of Equation 2.31;

$$\frac{1}{4\pi}\int_{4\pi}\int_{4\pi}\hat{s}\left(\Phi(\mathbf{r},t)P(\hat{s}',\hat{s})d\Omega'\right)d\Omega = \Phi(\mathbf{r},t)\int_{4\pi}\hat{s}[\int_{4\pi}P(\hat{s}',\hat{s})d\Omega']d\Omega = \Phi(\mathbf{r},t)\int_{4\pi}\hat{s}d\Omega = 0. \quad (2.32)$$

Note that $\int_{4\pi} P(\hat{s}', \hat{s}) d\Omega' = 1$. The second integral in Equation 2.31;

$$\int_{4\pi} \{\hat{s} \int_{4\pi} [\mathbf{J(r,t)} \cdot \hat{s'}] P(\hat{s}', \hat{s}) d\Omega'\} d\Omega = \int_{4\pi} [\int_{4\pi} \hat{s} P(\hat{s}', \hat{s})] [\mathbf{J(r,t)} \cdot \hat{s}'] d\Omega'. \tag{2.33}$$

In order to simplify Equation 2.33, we can apply to mathematical identify such that $\hat{s} = \hat{s}'(\hat{s}.\hat{s}) + \hat{s}' \times (\hat{s} \times \hat{s}')$. Then, we will be obtained two integrals.

By using the definition that is an anisotropy function, $g = \int_{4\pi} (\hat{s}.\hat{s}') P(\hat{s}', s) d\Omega$, first integral becomes

$$\int \hat{s}'(\hat{s}.\hat{s}') P(\hat{s}', s) d\Omega = \hat{s}' g. \tag{2.34}$$

The second integral becomes

$$\int \hat{s} \times (\hat{s} \times \hat{s}') P(\hat{s}', s) d\Omega = \hat{s}' \times [(\int_{4\pi} \hat{s} P(\hat{s}', s) d\Omega) \times \hat{s}']. \tag{2.35}$$

This integral is equal to zero because $P(\hat{s}', s)$ is parallel with $\hat{s}$, and its cross-product with $\hat{s}'$ is zero.

As a result of these steps mentioned above, the second part on the right hand side of Equation 2.27 is evaluated by using Equation 2.30

$$\begin{aligned} \frac{3}{4\pi} \int_{4\pi} \hat{s} [\int_{4\pi} [[\mathbf{J(r,t)} \cdot \hat{s}'] P(\hat{s}', \hat{s})] d\Omega' d\Omega = \\ g \frac{3}{4\pi} \int \hat{s}' [\mathbf{J(\ r,t)} \cdot \hat{s}'] d\Omega' = \frac{3}{4\pi} g \frac{4\pi}{3} \mathbf{J(r,t)} = g\mathbf{J(r,t)}. \end{aligned} \tag{2.36}$$

Finally, the source term can be written as $\int_{4\pi} \hat{s} S(\hat{r}, s, t) d\Omega = \frac{S(\hat{r},t)}{4\pi} \int_{4\pi} \hat{s} d\Omega = 0$.

After combining these parts, we have following Equation 2.37;

$$\frac{\partial \mathbf{J}(\mathbf{r},t)}{c\partial t} + \frac{1}{3}\nabla\Phi + \mu_t \mathbf{J}(\mathbf{r},t) = g\mu_s \mathbf{J}(\mathbf{r},t). \tag{2.37}$$

Note that $\mu_{s'} = (1-g)\mu_s$ and $\mu_t = \mu_a + \mu_s$. Furthermore, we can regularize Equation 2.37 step by step, and obtain Equation 2.40 which is the vector differential equation.

$$\frac{\partial \mathbf{J}(\mathbf{r},t)}{c\partial t} + \frac{1}{3}\nabla\Phi + (\mu_a + \mu_s)\mathbf{J}(\mathbf{r},t) = g\mu_s \mathbf{J}(\mathbf{r},t), \tag{2.38}$$

$$\frac{\partial \mathbf{J}(\mathbf{r},t)}{c\partial t} + \frac{1}{3}\nabla\Phi + \mu_a \mathbf{J}(\mathbf{r},t) + \mu_s(1-g)\mathbf{J}(\mathbf{r},t) = 0, \tag{2.39}$$

$$\frac{\partial \mathbf{J}(\mathbf{r},t)}{c\partial t} + \frac{1}{3}\nabla\Phi + (\mu_a + \mu_s')\mathbf{J}(\mathbf{r},t) = 0. \tag{2.40}$$

2.2.2. Second Approximation

We can assume that the time derivative of the flux is much smaller than the the interaction rate of the photons;

$$|\frac{\partial J(\mathbf{r},t)}{c\partial t}| \ll (\mu_a + \mu_s')\mathbf{J}(\mathbf{r},t). \tag{2.41}$$

In other words, the second approximation means that the photon current is temporally broadened with respect to transport mean free time. Indeed, the broadening results from a multiple-scattering event.

According to this approximation, time dependent term is ignored in Equation 2.40. Thus, this approximation leads to Fick's law, which states that the photon propagates from regions of high concentration to regions of low concentrations.

$$\mathbf{J(r,\ t)} = -D\nabla\Phi(\mathbf{r}, t) \tag{2.42}$$

where $D = \frac{1}{3(\mu_a+\mu_s')}$.

By substituting Fick's law equation into Equation 2.40, we obtain;

$$\frac{\partial\Phi(\mathbf{r}, t)}{c\partial t} + \mu_a\Phi(\mathbf{r}, t) - D\nabla^2\Phi(\mathbf{r}, t) = S(\mathbf{r}, t). \tag{2.43}$$

To sum up, these two approximations mentioned above are caused by a single condition which is $\mu_a \ll \mu_s'$.

2.2.3. Stochastic and Numerical Solutions to Diffusion Equation

There are several stochastic (statistical) methods such as Monte Carlo method, random walk theory, Markov fandom field theory. Monte Carlo method is the stochastic method, which widely is used to solve the diffusion equation. In 1983, this method was firstly introduced by Wilson [44]. This method is a flexible and it provides the most accurate solution compared with other numerical solutions. Although this method is computationally an efficient, the majority of the scientists apply to it in order to validate the results obtained by other models. Therefore, Monte Carlo method is called as a gold standard of the modeling light propagation in heterogenous media. This method depends on randomly the construction of a set of trajectories of photon

propagation in tissue. The step size and direction of each trajectory change according to absorption and scattering properties of tissue.

Numerical methods to solve the diffusion equation are finite difference, finite volume, finite element and boundary element approaches. Even though some articles concerning the finite difference method (FDM) [45, 46], finite volume method (FVM) [47], boundary element method (BEM) [48, 49] are available for some applications, FEM has become more appropriate numerical model.

3. THEORY OF IMAGE RECONSTRUCTION FOR DOT

Light does not propagate in human soft tissue in straight lines, in other words, light which travels in turbid medium (tissue) does not have the property of the ballistic. Therefore, imaging techniques (Radon transform and Backprojection method) which are used for X-ray CT are not feasible for DOT [17].

There are several models to predict light propagation within tissue such as analytical, stochastic, and numerical which mentioned above. Analytical solutions have the advantages of computationally being fast. Especially, Arridge *et al.* presented some specific analytical solutions for homogenous geometries in 1992 [50]. However, we are not able to use an an analytical model for heterogenous media. Considering numerical models; finite element, finite difference, finite volume, and boundary element are important models for complex heterogenous media. These numerical approaches have been used for the model based an image reconstruction in DOT. Thanks to these numerical approaches, a combination of DOT with a standard imaging system becomes feasible. The finite element is the common method for DOT image reconstruction algorithm. This method first was introduced for DOT by Arridge *et al.* [26, 51, 52].

Image reconstruction in NIR tomography is classified as two parts such as forward and inverse model [53].

3.1. Forward Model

The Boltzman transport Equation 2.16 represents the photon propagation in human tissue, and it simplifies in diffusion approximation equation under some specific assumptions. In order to tackle this equation, FEM is the most appropriate numerical model. This step is called forward problem. The solution of forward problem gives us to fluence rate.

3.1.1. FEM Reconstruction Algorithm

FEM is the technique for solving partial differential equation over a complicated domain [7]. Generally, this method constructs to non-linear relationship between the measurement and properties in the partial differential equation. Therefore, it is an appropriate technique to solve diffusion equation. FEM was first introduced into diffuse optical tomography by Arridge *et al.* [26]. According to this model, the fluence rate (photon density) is obtained with the help of set of boundary conditions and known values for μ_a and μ_s. We can summarize a finite reconstruction algorithm for DOT step by step [22]. Before interpreting FEM reconstruction algorithm, we must obtain diffusion equation in frequency domain system by using Fourier transform in time of Equation 2.43.

$$\nabla.D\nabla\Phi(\mathbf{r},\omega) - (\mu_a + \frac{i\omega}{c})\Phi(\mathbf{r},\omega) = -S(\mathbf{r},t) \tag{3.1}$$

where $\Phi(\mathbf{r},\omega)$ is defined as the photon density at position $\mathbf{r}$. Here, ω and $S(\mathbf{r},\omega)$ represent the light modulation frequency and isotropic source term, respectively. Additionally, $D = \frac{1}{3(\mu_a+\mu_{s'})}$ is defined as the optical diffusion coefficient.

(i) Appropriate finite element mesh can be generated. In other words, the geometry is meshed. This mesh subdivides geometry into elements. Thus, we can observe nodes. These nodes are located at the element corners and near each inside. Therefore, a set of triangular elements are observed. Each triangle represents an element as well as each vortex represents a node. In this case, the mesh can be defined as the number of nodes and elements. In DOT, the mesh represents the plane of the breast into a series of nodes.

To illustrate, the finite element mesh shown in Figure 3.1 with 1761 nodes and 3264 first order triangular elements was used by forward solver to calculate photon density at each node [54].

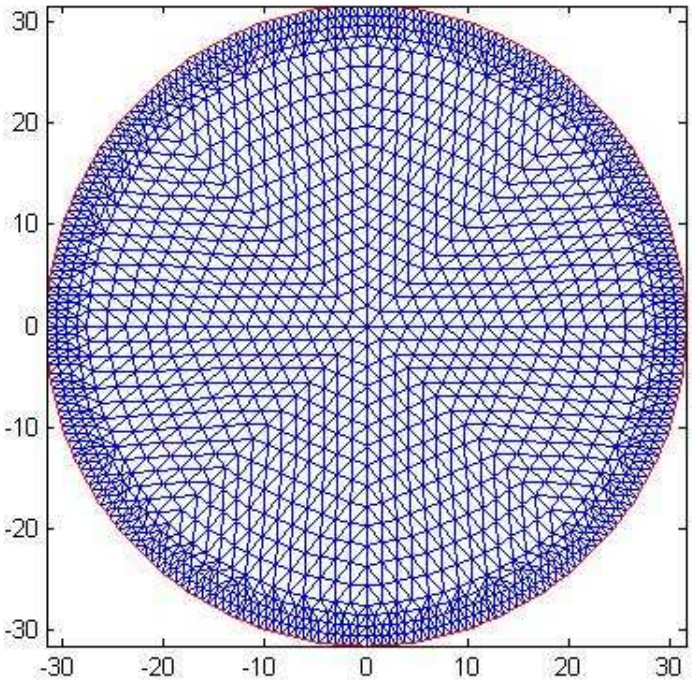

Figure 3.1. Finite Element Mesh (1761 nodes and 3264 first order triangular elements).

(ii) The source term and a set of boundary conditions as well as properties of the tissue are defined. The most important step for FEM reconstruction is to construct the weak form of the diffusion equation in the frequency domain system. In order to generate the weak form, we multiply Equation 3.1 with arbitrary test function φ and integrate for the two dimensional case.

$$\int\int(\nabla.D\nabla\Phi)\varphi dA - \int\int[(\mu_a + \frac{i\omega}{c})\Phi]\varphi dA = \int\int S\varphi dA. \tag{3.2}$$

By using the Green's theorem,

$$\int\int(\nabla.N)udA = \oint N.nuds - \int\int N.\nabla udA \tag{3.3}$$

where $N = D.\nabla\Phi$ and $u = \varphi$. We can simplify this equation as it follows

$$\oint(D\nabla\Phi.\vec{n})\varphi ds - \int\int D\nabla\Phi.\nabla\varphi dA - \int\int[(\mu_a + \frac{i\omega}{c})\Phi]\varphi dA = -\int\int S\varphi dA. \tag{3.4}$$

Furthermore, the test function is written for each node as function φ_i because we discretize the domain into a set of points and nodes. The relation between nodes in element is expressed by a basis function at each node. In this case, the test function refers to as a basis function. Additionally, the fluence rate can be discretized using the function Φ. This step can be expressed by Galerkin method [26]

$$\Phi = \sum_{j=1}^{N} \Phi_j\varphi_j \tag{3.5}$$

where N is defined as the total number of nodes.

$$\sum_{j=1}^{N} \Phi_j[-\langle D\nabla\varphi_j.\nabla\varphi_i\rangle - \langle(\mu_a + \frac{i\omega}{c})\varphi_j\varphi_i\rangle] = -\langle S\varphi_i\rangle - \sum_{j=1}^{M} D\nabla\Phi_j.\vec{n}\oint\varphi_j\varphi_i ds \tag{3.6}$$

where M is the number of boundary nodes.

We can use $\langle\ \rangle$ instead of integration over the problem domain.

Considering inhomogeneous medium, absorption and diffusion coefficients can be discretized, such that

$$\mu_a = \sum_{j=1}^{N} \mu_{aj}\varphi_j, \tag{3.7}$$

$$D = \sum_{j=1}^{N} D_j\varphi_j. \tag{3.8}$$

After these definitions, Equation 3.6 can be written as

$$\sum_{j=1}^{N} \Phi_j[-\langle D_k\varphi_k\nabla\varphi_j.\nabla\varphi_i\rangle - \langle(\sum_{k=1}^{N}(\mu_{ak}\varphi_k + \frac{i\omega}{c})\varphi_j\varphi_i = -\langle S\varphi_i\rangle + \sum_{j=1}^{M} D\nabla\Phi_j.\vec{n}\oint \varphi_j\varphi_i ds. \tag{3.9}$$

At this step, the boundary conditions can be used. The behavior of photon density of near the boundary of biological tissue is related to mixed Dirichlet-Neuman boundary condition [55].

In DOT, a boundary condition for RTE which suggests that we do not have photons which propagate in an inward direction at the boundary $\partial\Omega$ (Ω is the domain). This suggestion is not valid for the diffusion approximation [52], which is given by following Equation 3.10.

$$L(\mathbf{r}, \hat{s}) = 0, \quad \mathbf{r}\epsilon\partial\Omega, \quad \hat{n} < 0 \tag{3.10}$$

where $\hat{n}$ is outward unit normal. Instead of this boundary condition, Robin boundary

condition in DOT is used. We derive as follows [56, 57].

The measurable quantity which is the exitance can be written as

$$\Gamma(r) = \int_{S^{m-1}} L(\mathbf{r}, \hat{s})(\hat{s} \cdot \hat{n}) d\hat{s} \quad \mathbf{r} \epsilon \partial\Omega \tag{3.11}$$

where $|S^{m-1}|$ denotes the surface measure of the sphere. The total inward directed photon flux at a point r on the boundary is expressed as

$$\Gamma_{-}(r) = \int_{\hat{s}\cdot\hat{n}<0} L(\mathbf{r}, \hat{s})(\hat{s} \cdot \hat{n}) d\hat{s}. \tag{3.12}$$

For the outward directed photon flux at a point $r \epsilon \partial\Omega$

$$\Gamma_{+}(r) = \int_{\hat{s}\cdot\hat{n}>0} L(\mathbf{r}, \hat{s})(\hat{s} \cdot \hat{n}) d\hat{s} \tag{3.13}$$

is written. These two integrals above can be calculated. In general, radiance is written as;

$$L(\mathbf{r}, \hat{s}) \approx \frac{1}{|S^{m-1}|}\Phi(\mathbf{r}) + \frac{m}{|S^{m-1}|}\mathbf{J(r)} \cdot \hat{s}. \tag{3.14}$$

Therefore;

$$\Gamma_{-}(r) = \int_{\hat{s}\cdot\hat{n}<0} L(\mathbf{r}, \hat{s})(\hat{s} \cdot \hat{n}) d\hat{s} \approx \int \{\frac{\Phi(\mathbf{r})}{|S^{m-1}|} + \frac{m}{|S^{m-1}|}\mathbf{J(r)}\} \cdot \hat{s}(\hat{s} \cdot \hat{n}) d\hat{s} \tag{3.15}$$

and

$$\Gamma_{-}(r) = \frac{\Phi(\mathbf{r})}{|S^{m-1}|} \int (\hat{s} \cdot \hat{n}) d\hat{s} + \frac{m}{|S^{m-1}|} \int (\hat{s} \cdot \hat{n}) \hat{s} \cdot \mathbf{J(r)} d\hat{s}. \tag{3.16}$$

For the first integral; $\int(\hat{s}\cdot\hat{n})ds = -|S^{m-2}|\int_0^1 t(1-t^2)^{(n-3)/2}dt = -\frac{|S^{m-2}|}{m-1}$.

Here, the photon flux is divided into two parts; perpendicular and parallel to the surface $\partial\Omega$; $\mathbf{J} = (\mathbf{J}\cdot\hat{n})\hat{n} + \hat{n}\mathbf{J}_\perp$, $\hat{n}\cdot\mathbf{J}_\perp = 0$. Then, the second integral;

$$\int_{\hat{n}\cdot\hat{s}<0}(\mathbf{J}\cdot\hat{s})(\hat{s}\cdot\hat{n})d\hat{s} = (\mathbf{J}\cdot n)\int_{\hat{s}\cdot\hat{n}<0}(\hat{n}\cdot\hat{s})^2 ds + \int(\hat{s}\mathbf{J}_\perp)(\hat{s}\cdot\hat{n})ds, \tag{3.17}$$

$$\int(\hat{s}\cdot\hat{n})^2 ds = \frac{1}{2}\int_{S^{m-1}}(\hat{n}\cdot\hat{s})^2 ds = \frac{|S^{m-1}|}{2m} \tag{3.18}$$

where $|S^{m-1}| = \frac{(2\pi)^{\frac{m}{2}}}{\Gamma(\frac{m}{2})}$,

$$\Gamma_-(r) = \frac{1}{|S^{m-1}|}(-\frac{|S^{m-2}|}{m-1}\Phi + m(\mathbf{J}\cdot\hat{n})\frac{S^{m-1}}{2m}) = -\gamma\Phi + \frac{1}{2}\hat{n}\cdot\mathbf{J} \tag{3.19}$$

where $\gamma = \gamma_m = \frac{\Gamma(\frac{m}{2})}{\sqrt{\pi}(m-1)\Gamma(\frac{m-1}{2})}$,

$$\Gamma_-(r) = \int_{\hat{s}\cdot\hat{n}<0} L(\mathbf{r},\hat{s})(\hat{s}\cdot\hat{n})d\hat{s} = -\gamma\Phi(r) + \frac{1}{2}\hat{n}\cdot J(\mathbf{r}). \tag{3.20}$$

By the same way, we can calculate the outward directed photon flux;

$$\Gamma_+(r) = \int_{\hat{s}\cdot\hat{n}>0} L(\mathbf{r},\hat{s})(\hat{s}\cdot\hat{n})d\hat{s} = \gamma\Phi(r) + \frac{1}{2}\hat{n}\cdot\mathbf{J(r)}. \tag{3.21}$$

Furthermore, we can assume that the total inward directed photon flux on the boundary is zero such that $\Gamma_-(r) = 0, \qquad r\epsilon\partial\Omega$.

$$\gamma\Phi(r) - \frac{1}{2}\hat{n} \cdot J(r) = 0. \tag{3.22}$$

By using Fick's law Equation 2.42 in Equation 3.22, we obtain the Robin boundary condition.

$$\Phi(r) + \frac{1}{2\gamma}D\frac{\partial\Phi(r)}{\partial n} = 0 \quad r\epsilon\partial\Omega. \tag{3.23}$$

We can also incorporate a mismatch between refractive indices on domain and the surrounding medium such that

$$\int_{\hat{s}\cdot\hat{n}<0} L(\mathbf{r},\hat{s})(\hat{s}\cdot\hat{n})d\hat{s} = \int_{\hat{s}\cdot\hat{n}>0} R(\hat{s})L(\mathbf{r},\hat{s})(\hat{s}\cdot\hat{n})d\hat{s}. \tag{3.24}$$

Thus, we obtain modified Robin boundary condition

$$-\gamma\Phi(r) + \frac{1}{2}D\frac{\partial\Phi(r)}{\partial n} = R(\hat{s})[\gamma\Phi(r) + \frac{1}{2}D\frac{\partial\Phi}{\partial n}], \tag{3.25}$$

$$\Phi(r) + \frac{1}{2\gamma}\beta D\frac{\partial\Phi}{\partial n} = 0 \tag{3.26}$$

where $\beta = \frac{1+R}{1-R}$.

In the diffusion approximation framework, the exitance is expressed as

$$\Gamma(r) = \Gamma_{+}(r) - (-\Gamma_{-}(r)) = \hat{n} \cdot J(r)$$

$$= -D\frac{\partial\Phi(r)}{\partial n} = \frac{2\gamma}{A}\Phi(r), \quad r\epsilon\partial\Omega. \tag{3.27}$$

$$\mathbf{J}\cdot\hat{n} = -D\nabla\Phi\cdot\hat{n} = \alpha\Phi \tag{3.28}$$

where $\alpha = \frac{2\gamma}{\beta}$. After obtaining Robin boundary condition, it is used in following equation which mentioned above Equation 3.9.

$$\sum_{j=1}^{N}\Phi_j[-\langle D_k\varphi_k\nabla\varphi_j.\nabla\varphi_i\rangle - \langle(\sum_{k=1}^{N}(\mu_{ak}\varphi_k + \frac{i\omega}{c})\varphi_j\varphi_i\rangle = -\langle S\varphi_i\rangle + \alpha\sum_{j=1}^{M}\Phi_j\oint\varphi_j\varphi ids, \tag{3.29}$$

$$\begin{aligned}\sum_{k=1}^{M}\Phi_j[-\langle D_k\varphi_k\nabla\varphi_j.\nabla\varphi_i\rangle - \langle(\sum_{k=1}^{N}(\mu_{ak}\varphi_k + \frac{i\omega}{c})\varphi_j\varphi_i\rangle + \alpha\oint\varphi_j\varphi_i] + \\ \sum_{j=M+1}^{N}\Phi_j[-\langle D_k\varphi_k\nabla\varphi_j.\nabla\varphi_i\rangle - \langle(\sum_{k=1}^{N}(\mu_{ak}\varphi_k + \frac{i\omega}{c})\varphi_j\varphi_i\rangle] = \langle S\varphi_i\rangle.\end{aligned} \tag{3.30}$$

This Equation 3.30 can be shown by matrix representation (see Equation 3.31) that is the traditional FEM solution [22].

$$\begin{bmatrix} A_{bb} & A_{bI} \\ A_{Ib} & A_{II} \end{bmatrix}\begin{bmatrix} \Phi_b \\ \Phi_I \end{bmatrix} = \begin{bmatrix} S_b \\ S_I \end{bmatrix} \tag{3.31}$$

where

$$a_{ij}^{bb} = -\langle D_k\varphi_k\nabla\varphi_j.\nabla\varphi_i\rangle - \langle(\sum_{k=1}^{N}(\mu_{ak}\varphi_k + \frac{i\omega}{c})\varphi_j\varphi_i\rangle + \alpha\oint\varphi_j\varphi_i ds, \tag{3.32}$$

$$a_{ij}^{bI} = a_{ij}^{Ib} = a_{ij}^{II} = -\langle \sum_{k=1}^{N} D_k \varphi_k \nabla \varphi_j . \nabla \varphi_i \rangle - \langle (\sum_{k=1}^{N} \mu_{ak} \varphi_k + \frac{i\omega}{c}) \varphi_j \varphi_i \rangle, \tag{3.33}$$

$$S_i^b = S_i^I = -\langle S \varphi_i \rangle. \tag{3.34}$$

These integrals rely on the mesh, geometry, optical properties throughout the mesh. Because of using linear elements, the matrix A can be calculated. Additionally, we obtain photon density Φ by this way; $\Phi = A^{-1}S$.

To sum up, the solution to forward problem enables to obtain the photon density everywhere relied on known values for μ_a and $\mu_{s'}$ at each FEM nodes after definition set of boundary conditions and particular source. Therefore, this photon density obtained from forward problem is called as calculated photon density.

3.2. Inverse Problem

The purpose of the setting inverse problem is the recovery of the unknown optical properties with the help of measured data. Random assumptions of optical properties provide us with calculation of the photon density. In order to obtain accurate optical properties, we count difference between measured and calculated photon density rather than choosing another random assumption.

The measured data obtaining from frequency domain system consists of the amplitude (A) and phase (θ) of transmitted signal. Furthermore, we define the amplitude and phase resulting from calculated photon density such that $A = \sqrt{Re(\Phi(\mu))^2 + Im(\Phi(\mu))^2}$ and $\theta = \tan^{-1} \frac{Im(\Phi(\mu)}{Re(\Phi(\mu))}$ where $\mu = [D(r); \mu_a(r)]$ [58].

DOT has a poor spatial resolution owing to the dominance of light scattering in soft tissue over the absorption. Therefore, DOT inverse problem is a non-linear. In other words, if we change optical properties linearly, we does not obtain linear changes in the detected signals, which is called as ill-posed problem [52].

Generally, ill-posedness is the typical mathematical property of inverse problem. This type of problem possesses a non-unique solution, and the data which belongs to ill-posed problem is not continuous. Inverse problem does not have stable solution. In this case, smaller changes in the detected signals cause large changes in assumed optical properties. Additionally, an inverse problem is ill-conditioned or ill- determined [59]. When the number of measurements is not equal to the number of unknowns, then the problem is called as ill-conditioned. Especially, this situation occurs in the case of measurements for heterogenous media (biological tissue) [60]. When considering these detrimental properties, inverse problem in DOT is called as a non-uniqueness problem. In order to get rid of this undesirable situation, some techniques are suggested. For illustrate, we should become aware of choosing measurements, or minimize noise and errors in the measurements. However, these two techniques are difficult. The other feasible way to tackle ill-conditioned problem is numerical methods. We can obtain an approximate solution from inverse problem. This approach is called regularization methods for the solution of ill-posed problems, which is called as golden rule [59]. The important property of the regularization methods is the use of additional information. In DOT, inverse problem is based on minimizing an objective function such that the difference between calculated data and observed data, $\chi^2 = \|\Phi_c - \Phi_m\|$. There are three types of minimization techniques; Levenberg-Marquardt, Tikhonov-Minimization and Generalized Least Squares (GLS) minimization. We will discuss some of these techniques, Lavenberg-Marquardt and Tikhonov Minimization, and determine which technique is the most appropriate for the inverse problem for DOT in the following section.

3.2.1. Minimization Techniques

Several research groups utilize a structural information obtaining from other imaging modalities such as X-ray mammography, Ultrasound and MRI [61]. Because of advantage of multi-modality image data, the interest in using priori information in DOT has risen and some different techniques have been suggested in inverse problem. In this case, minimization techniques such as Levenberg-Marquardt and Tikhonov approaches are modified with respect to without spatial priors and with spatial priors [58].

3.2.1.1. Levenberg-Marquardt. The LM method is enhanced Gauss-Newton method which minimizes the traditional sum of square objective function. Because Gauss-Newton method does not overcome ill-posedness, Lavenberg- Marquardt implemented λ in order to modify the object function. Firstly, we can define an objective function for DOT as $\chi^2 = \Sigma_{i=1}^{NM} \|(\Phi_i^C - \Phi_i^M)\|^2$ where Φ_i^M is the measured data or measured photon density, Φ_i^C is the calculated data resulting from forward problem, and NM is the total number of measurements

$$\chi^2 = \Sigma_{i=1}^{NM} \|(\Phi_i^C - \Phi_i^M)\|^2. \tag{3.35}$$

According to Newton's method, $\frac{\partial \chi^2}{\partial \mu}$ is expanded for nearby point μ_0;

$$\frac{\partial \chi^2}{\partial \mu} = \frac{\partial \chi^2}{\partial \mu}(\mu_0) + (\mu - \mu_0)\frac{d}{d\mu}(\frac{\partial \chi^2}{\partial \mu}(\mu_0)) + ... \tag{3.36}$$

We can use $\mu - \mu_0$ instead of $\mu_{i+1} - \mu_i$ and assume that $\frac{\partial \chi^2}{\partial \mu} \approx 0$. Thus, we obtain the Standard Newton Rapson iterative form;

$$\mu_{i+1} = \mu_i + [\frac{d}{d\mu}(\frac{\partial \chi^2}{\partial \mu}\mu_i)]^{-1}(\frac{\partial \chi^2}{\partial \mu})(\mu_i). \tag{3.37}$$

We can calculate derivative terms;

$$\frac{\partial \chi^2}{\partial \mu}(\mu_i) = \frac{\partial}{\partial \mu}[(\Phi_i^C - \Phi_i^M)^T(\Phi_i^C - \Phi_i^M)]. \tag{3.38}$$

Here, we use this following mathematical equation;

$$\frac{\partial (u^T V)}{\partial x} = u^T \frac{\partial V}{\partial x} + V^T \frac{\partial u}{\partial x} \tag{3.39}$$

where $u = u(x)$ and $V = V(x)$. Thus;

$$\begin{aligned} \frac{\partial \chi^2}{\partial \mu}(\mu_i) &= (\Phi_i^C - \Phi_i^M)^T \frac{\partial \Phi_i^C}{\partial \mu} + (\Phi_i^C - \Phi_i^M)^T \frac{\partial \Phi_i^C}{\partial \mu} \\ &= 2(\Phi^C - \Phi^M)^T (\frac{\partial \Phi^C}{\partial \mu}) = 2(\frac{\partial \Phi^C}{\partial \mu})^T (\Phi^C - \Phi^M), \end{aligned} \tag{3.40}$$

$$\frac{\partial}{\partial \mu}(\frac{\partial \chi^2}{\partial \mu}\mu_i) = 2(\frac{\partial \Phi^C}{\partial \mu})^T \frac{\partial \Phi^C}{\partial \mu} + 2(\frac{\partial^2 \Phi}{\partial^2 \mu})^T (\Phi^C - \Phi^M), \tag{3.41}$$

and we can ignore the second derivative term in Equation 3.41. Substituting Equations 3.40 and 3.41 into equation of Standard Newton Rapson Equation 3.37, we obtain

$$\mu_{i+1} = \mu_i + [(\frac{\partial \Phi^C}{\partial \mu})^T (\frac{\partial \Phi}{\partial \mu})]^{-1} (\frac{\partial \Phi}{\partial \mu})^T (\Phi^C - \Phi^M) \tag{3.42}$$

and

$$\Delta \mu = (J^T J)^{-1} J^T (\Phi^C - \Phi^M) \tag{3.43}$$

where $\Delta \mu = \mu_{i+1} - \mu_i$, the derivative matrix $(\frac{\partial \Phi^C}{\partial \mu})$ is the Jacobian matrix. Additionally,

Jacobian matrix is called as a sensitivity, or weight matrix. This matrix defines the relationship between changes in modeled data Φ^C due to the small changes in optical properties $\mu = (\mu_a, D)$.

Considering the frequency domain data, we get an amplitude and a phase of the signal. Furthermore, the problem is related to the effects of absorption and diffusion. Thus, the Jacobian matrix is constructed as follows;

$$J = \begin{bmatrix} \frac{\delta \ln I_1}{\delta D_1} & \frac{\delta \ln I_1}{\delta D_2} & \cdots & \frac{\delta \ln I_1}{\delta D_{NN}}; & \frac{\delta \ln I_1}{\delta \mu_{a1}} & \frac{\delta \ln I_1}{\delta \mu_{a2}} & \cdots & \frac{\delta \ln I_1}{\delta \mu_{aNN}} \\ \frac{\delta \theta_1}{\delta D_1} & \frac{\delta \theta_1}{\delta D_2} & \cdots & \frac{\delta \theta_1}{\delta D_{NN}} & \frac{\delta \theta_1}{\delta \mu_1} & \frac{\delta \theta_1}{\delta \mu_2} & \cdots & \frac{\delta \theta_1}{\delta \mu_{NN}} \\ \frac{\delta \ln I_2}{\delta D_1} & \frac{\delta \ln I_2}{\delta D_2} & \cdots & \frac{\delta ln I_2}{\delta D_{NN}} & \frac{\delta \ln I_2}{\delta \mu_{a1}} & \frac{\delta \ln I_2}{\delta \mu_{a2}} & \cdots & \frac{\delta \ln I_2}{\delta \mu_{aNN}} \\ \frac{\delta \theta_2}{\delta D_1} & \frac{\delta \theta_2}{\delta D_2} & \cdots & \frac{\delta \theta_2}{\delta D_{NN}} & \frac{\delta \theta_2}{\delta \mu_{a1}} & \frac{\delta \theta_2}{\delta \mu_{a2}} & \cdots & \frac{\delta \theta_2}{\delta \mu_{NN}} \\ \vdots & \vdots & \ddots & \vdots & \vdots & \vdots & \ddots & \vdots \\ \frac{\delta ln I_{NM}}{\delta D_1} & \frac{\delta \ln I_{NM}}{\delta D_2} & \cdots & \frac{\delta \ln I_{NM}}{\delta D_{NN}} & \frac{\delta \ln I_{NM}}{\delta \mu_{a1}} & \frac{\delta \ln I_{NM}}{\delta \mu_{a2}} & \cdots & \frac{\delta \ln I_{NM}}{\delta \mu_{aNN}} \\ \frac{\delta \theta_{NM}}{\delta D_1} & \frac{\delta \ln I_{NM}}{\delta D_2} & \cdots & \frac{\delta \theta_{NM}}{\delta D_{NN}} & \frac{\delta \theta_{NM}}{\delta \mu_{a1}} & \frac{\delta \theta_{NM}}{\delta \mu_{a2}} & \cdots & \frac{\delta \theta_{NM}}{\delta \mu_{aNN}} \end{bmatrix} \tag{3.44}$$

where $\frac{\delta \ln I_i}{\delta D_i}$ and $\frac{\delta \ln I_i}{\delta \mu_{a_j}}$ represent the change in log of amplitude of ith measurement resulting from a small change in D and μ_a at the jth reconstructed point respectively. Furthermore, $\frac{\delta \theta_i}{\delta D_j}$ and $\frac{\delta \theta_i}{\delta \mu_{aj}}$ define the change in phase of ith measurement resulting from a change in D and μ_a at the jth node respectively [62]. This matrix is constructed by adjoint method which is associated with reciprocity theorem [63].

It is unfortunate that the jacobian matrix is "fat" matrix, in other words, the number of rows is smaller than that of columns. Therefore, $J^T J$ is ill-conditioned. In order to tackle this detrimental problem, regularization term, the quantity to diagonal of $J^T J$, is added into Equation 3.43.

$$\Delta\mu = (J^T J + \lambda I)^{-1} J^T (\Phi^C - \Phi^M), \tag{3.45}$$

where I is an identity matrix. λI stabilizes the matrix inversion. The first value of the (λ) is the ratio of the variances and is decreased at each of the iteration by a small factor [64]. According to pseudo inversion [65], Equation 3.45 is written in other form as

$$\Delta\mu = J^T(JJ^T + \lambda I)^{-1}(\Phi^C - \Phi^M). \tag{3.46}$$

The Equation 3.46 which recovers the optical properties is more suitable than the Equation 3.45 because the number of unknown is much larger than the amount of measurements. If the sensitivity matrix (J) were "skinny matrix", the number of rows is greater than that of the columns, we would use Equation 3.45 in the reconstruction algorithms [66]. Even though both Equations 3.45 and 3.46 are equal in terms of mathematical, the latter solves smaller and better conditioned matrix because of the property of the Jacobian matrix. Forward problem is solved by using a fine mesh which is shown in the Figure 3.1. However, this mesh is not sufficient for inverse problem of DOT. For instance, in order to reduce the number of unknowns in matrix Equation 3.46, the coarser mesh with 289 nodes and 512 first order triangular elements (see Figure 3.2) was constructed according to the fine mesh and used for inverse problem by using MATLAB (matrix laboratory) software [54].

3.2.1.2. Tikhonov-Minimization. The Tikhonov-Minimization technique is different from Laevenberg-Marquardt minimization in terms of having a modified object function.

$$\chi^2 = \Sigma_{i=1}^{NM}\|(\Phi_i^C - \Phi_i^M)\|^2 + \lambda\sum_{j=1}^{NM}\|(L(\mu_j - \mu_0))\|^2 \tag{3.47}$$

where λ is the Tikhonov regularization parameter and L is the dimensionless regularization matrix which is generated by other imaging modalities like MRI.

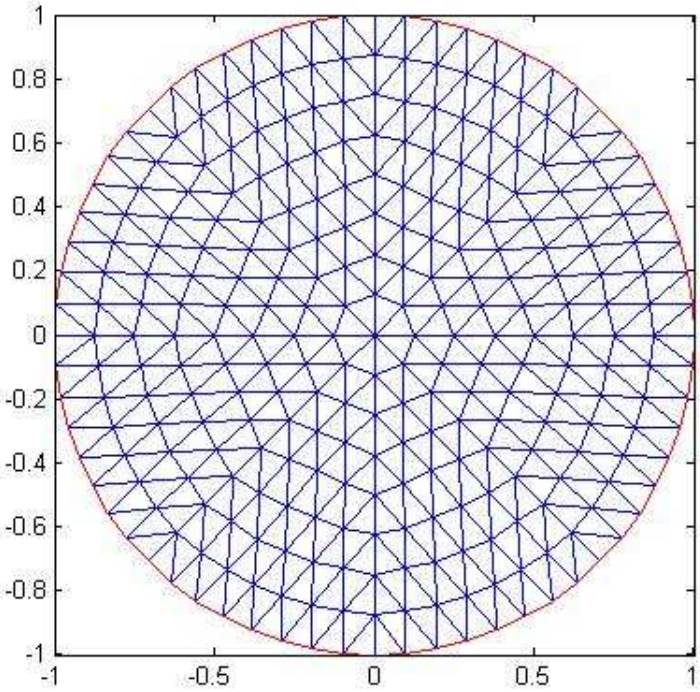

Figure 3.2. Finite Element Mesh (289 nodes and 512 first order triangular elements).

$$\chi^2 = \{\frac{\Sigma_{i=1}^{NM}\|(\Phi_i^C - \Phi_i^M)\|^2}{(\sigma_{\Phi^M})^2} + \frac{\sum_{j=1}^{NM}\|(\mu_j - \mu_0)\|^2)}{(\sigma_{\mu_j-\mu_0})^2}\}, \tag{3.48}$$

where σ_{Φ^M} is the standard deviation in the data Φ^C and $\sigma_{\mu_j-\mu_0}$ is the standard deviation in optical properties. $((\sigma_{\mu_j-\mu_0})^2 = (\sigma_{\Phi^M})^2 + (\sigma_{\Phi^M})^2$ with $(\sigma_{\Phi^M}^2) = 0)$. After multiplying Equation 3.48 by $\sigma_{\Phi^M}^2$, we can compare Equations 3.47 and 3.48. Thus, we obtain Tikhonov regularization parameter such that $\lambda = (\frac{\sigma_{\Phi^M}}{\sigma_{\mu_j-\mu_0}})$.

The Newton-Rapson Iterative form mentioned above is

$$\mu_{i+1} = \mu_i + \frac{d}{d\mu}(\frac{\partial\chi^2}{\partial\mu}\mu_i)^{-1}(\frac{\partial\chi^2}{\partial\mu})(\mu_i). \tag{3.49}$$

We can calculate derivative terms in the Equation 3.49 with the aid of the Equation 3.39;

$$\frac{\partial \chi^2}{\partial \mu}(\mu_i) = 2(\frac{\partial \Phi^C}{\partial \mu})^T(\Phi^C - \Phi^M) + 2\lambda L^T L(\mu_j - \mu_0), \tag{3.50}$$

$$(\frac{\partial}{\partial \mu})(\frac{\partial \chi^2}{\partial \mu}\mu_i) = 2(\frac{\partial \Phi^C}{\partial \mu})^T\frac{\partial \Phi^C}{\partial \mu} + 2(\frac{\partial^2 \Phi}{\partial^2 \mu})^T(\Phi^C - \Phi^M) + 2\lambda L^T L, \tag{3.51}$$

and we can ignore the second derivative term in Equation 3.51. Substituting Equations 3.50 and 3.51 into Equation 3.49 of Standard Newton Rapson iterative form, we obtain

$$\Delta\mu = (J^T J + \lambda L^T L)^{-1}[J^T(\Phi^C - \Phi^M) + \lambda L^T L(\mu_j - \mu_0)] \tag{3.52}$$

where the derivative matrix $(\frac{\partial \Phi^C}{\partial \mu})$ is the Jacobian matrix which is constructed in the previous section. Here, L matrix is formed by prior spatial information. If we do not have spatial priors, L can be constructed as the identity matrix. L matrix, which is called as the penalty term, includes in a priori information in DOT. Thus, the image reconstruction is improved by λ in terms of the sensitivity of a reconstruction method.

When a higher modulation frequency is used, we obtain a better separation of absorption and scattering properties [67]. Additionally, the increase of the frequency results in a better discrimination between normal and tumor tissue [68]. Considering this information, M. B. Ünlü *et al.* improved the image quality by the use of two-frequency data instead of one frequency data. In order to demonstrate that, he applied to Multiparameter Tikhonov regularization [54]. In this case, the Jacobian matrix is formed by each frequency such that

$$\tilde{J} = \begin{bmatrix} J(\omega 1) \\ J(\omega) \\ J(\omega 3) \\ \vdots \\ J(\omega_f) \end{bmatrix} , \tag{3.53}$$

where f is the number of frequencies and $J(\omega_i)$ represents the jacobian matrix which is constructed by each frequency. Furthermore, the difference between modulated data and measured data change with regard to multi-frequency data;

$$(\tilde{\Phi}_m - \tilde{\Phi}_c) = \begin{bmatrix} (\tilde{\Phi}_m(\omega_1) - \tilde{\Phi}_c(\omega_1) \\ (\tilde{\Phi}_m(\omega_2) - \tilde{\Phi}_c(\omega_2)) \\ (\tilde{\Phi}_m(\omega_3) - \tilde{\Phi}_c(\omega_3)) \\ \vdots \\ (\tilde{\Phi}_m(\omega_f) - \tilde{\Phi}_c(\omega_f)) \end{bmatrix} . \tag{3.54}$$

Thus, the matrix equation which gives use optical properties of tissue is written as

$$\Delta\mu = \tilde{J}^T(\tilde{J}^T\tilde{J} + \lambda I)^{-1}(\tilde{\Phi}^C - \tilde{\Phi}^M). \tag{3.55}$$

3.2.2. A Priori Information

There is a significant interest in developing hybrid systems. One of the hybrid systems is the combined MRI-DOT. To overcome the low resolution in DOT, researchers suggested different ways of penalizing the objective function with a structural information. This priori information optimizes recovery of a stimulated optical

property distribution. These techniques were first suggested by Barbour *et al.* [69], and Schweiger *et al.* [70]. In the literature, there are underlying studies which consist of NIR tomography with a priori structural information. Ntziachristos *et al.* separated the imaging domain into tumor and non-tumor regions with the help of the priori structural information from MRI, and provided well posed problem [71]. Furthermore, Li *et al.* benefited from X-ray tomosynthesis so as to divide the breast into different subregions and proposed different regularization parameters according to these volumes. In recent years, Pogue and Paulsen [72], Brooksby *et al.* [73] and Yalavarthy *et al.* [74] improved some methods for utilizing of an anatomical priori information.

Taking an information derived from other modalities, especially MRI, into consideration, it is needed to have a superior reconstruction NIR image quality. In this regard, least square minimization algorithm can be divided into two approaches; hard-priors and soft priors.

3.2.2.1. Hard-Priors. Hard priors approach can be called as a parameter reduction technique. In the hard-priori application, Jacobian matrix is regulated in according with reduction of parameter space to the number of regions derived from a high resolution imaging modality. In hard-prior method, a structural segmentation derived from other imaging modalities includes single values of optical properties, μ_a and $\mu_{s'}$. This priori information constructs to the new Jacobian matrix. In this case, the dimension of Jacobian matrix becomes (2*NM)x(2*NR) instead of (2*NM)x(2*NN). In here; NM, NN, NR define the number of measurements, number of FEM nodes, and number of regions respectively. Furthermore, the multiplication factor 2 in dimensions represents the concept of the amplitude and phase separately for the frequency domain system. A new jacobian matrix is represented by $\tilde{J} = JM$. In this case, the dimension of the M which is the priori matrix becomes (2*NN)x(2*NR) [58]. Here, M represents the priori matrix;

$$M = \begin{bmatrix} k_{1,1} & k_{1,2} & \cdots & k_{1,n} \\ k_{2,1} & k_{2,2} & \cdots & k_{2,n} \\ \vdots & \vdots & \ddots & \vdots \\ k_{j,1} & k_{j,2} & \cdots & k_{j,n} \\ \\ k_{2,1} & k_{2,2} & \cdots & k_{2,n} \\ \\ k_{1,1} & k_{1,2} & \cdots & k_{1,n} \\ k_{2,1} & k_{2,2} & \cdots & k_{2,n} \\ \vdots & \vdots & \ddots & \vdots \\ k_{j,1} & k_{j,2} & \cdots & k_{j,n} \end{bmatrix} \tag{3.56}$$

where $k_{\alpha,\gamma} = \begin{cases} 1, & \alpha \in R_\gamma \\ 0, & \alpha \notin R_\gamma. \end{cases}$

The columns of "M" matrix indicate the information of regions obtaining from MRI.

Using a hard priori information, we can write the following matrix equation which enables us to obtain optical properties of tissue.

$$\Delta\mu = (\tilde{J}^T\tilde{J})^{-1}\tilde{J}^T(\Phi^C - \Phi^M). \tag{3.57}$$

In order to evaluate this matrix Equation 3.57, a regularization term is not necessary because the number of measurement is greater than the number of regions. This matrix $(\tilde{J})$ is called as a well-conditioned matrix.

There are some drawbacks and advantages of this method. On one hand, it

is overdetermined because $J^T J$ is a positive definite, on the other hand, it may not overcome an undesirable property, which is ill-posed, of DOT. Furthermore, it is computationally efficient. Pogue and Paulsen applied to a hard prior and demonstrated that this method contributes to a simulated optical property reconstruction [72].

3.2.2.2. Soft-Priors. In this method, the regularization matrix L mentioned above is formed in the Tikhonov approach. There are two forms of the L-matrix, which are a Laplacian-type structured regularization matrix and a Helmholtz-type structured regularization matrix. L matrix is generated according to some regions which are determined by a priori information. In other words, L matrix represents labeled nodes in FEM mesh determined by the region and tissue type.

$$L = \begin{bmatrix} l_{1,1} & \cdots & l_{1,NN} & \downarrow & & & \\ \vdots & \ddots & & \downarrow & & 0 & \\ l_{NN,1} & & l_{NN,NN} & \downarrow & & & \\ \longrightarrow & \longrightarrow & \longrightarrow & \longrightarrow & \longrightarrow & \longrightarrow & \longrightarrow \\ & & & \downarrow & l_{1,1} & \cdots & l_{1,NN} \\ & 0 & & \downarrow & \cdots & \ddots & \\ & & & \downarrow & l_{NN,1} & & l_{NN,NN} \end{bmatrix} \tag{3.58}$$

$$\text{where } l_{i,j} = \begin{cases} 1, & i = j \\ \frac{-1}{N}, & R_i = R_j \\ 0, & R_i \neq R_j. \end{cases}$$

According to the Laplacian-type structured regularization matrix, L matrix is given by

$$L_{i,j} = \begin{cases} 0 & if \;\; i \;\; and \;\; j \;\; are \;\; not \;\; in \;\; the \;\; same \;\; region \\ \frac{-1}{N} & if \;\; i \;\; and \;\; j \;\; are \;\; in \;\; the \;\; same \;\; region \\ 1 & if \;\; i = j \end{cases} \tag{3.59}$$

where N is the number of finite element mesh nodes.

Furthermore, L matrix can be generated by a Helmholtz-type structured regularization matrix;

$$L_{i,j} = \begin{cases} 0 & if \;\; i \;\; and \;\; j \;\; are \;\; not \;\; in \;\; the \;\; same \;\; region \\ \frac{-1}{N+(kh)^2} & if \;\; i \;\; and \;\; j \;\; are \;\; in \;\; the \;\; same \;\; region \\ 1 & if \;\; i = j \end{cases} \tag{3.60}$$

where h is the distance between the nodes, $k = \frac{1}{l}$ represents the inverse of the size of the tumor in the domain [58].

4. COMBINED DIFFUSE OPTICAL TOMOGRAPHY (DOT) and MRI SYSTEM FOR CANCER IMAGING IN SMALL ANIMALS

In medical imaging, one imaging system which possesses high resolution may contribute to another imaging system which possesses a good contrast resolution. Combined DOT-MRI imaging system is one of the most important examples of this situation. These two imaging modalities which use non-ionizing techniques enable us to obtain structural and functional information about tissue. provide structural and functional physiological information. Thus, this complementary technique gives us an information about characterization of tumors. Furthermore, this hybrid system is applied for understanding the impact of neoadjuvant chemotherapies [75]. Before comprehending coregistration of these two methods, we can give a brief information about working principle of MRI in terms of physics.

4.1. The Basic Physics of MRI

MRI is associated with magnetic property of tissue. The first MR image was made by Paul C. Lauterbur by representing gradients in the magnetic field in 1973. Subsequently, Peter Mansfield introduced the mathematical theory for fast scanning and an image reconstruction. However, the physical theory based on the laws of Newton and Maxwell is not sufficient for the principles of MRI. After demonstration of the special theory and relativity in 1905, the theory of the quantum mechanics was enhanced and the atomic and subatomic scale were interpreted. Thus, the property of spin angular momentum which consists of description of NMR was comprehended by the special theory of relativity and quantum mechanics [76].

MR imaging is generated by the signal coming from the protons in the nuclei of hydrogen atoms resulting from water molecules in the body. These protons which have spin behave like tiny magnets in the strong magnetic field. Before the strong

magnetic field is applied to protons, they are randomly oriented. In the presence of the external magnetic fields, alignment of the some of spinning protons' direction will be same with the direction of the magnetic field. On the other hand, some of them will attempt to adjust to opposite direction of the magnetic field. In other words, spin which is exposed to an external magnetic field alters the orientation of its rotational axis [77]. This event is called a precession. In this regard, longitudinal magnetization

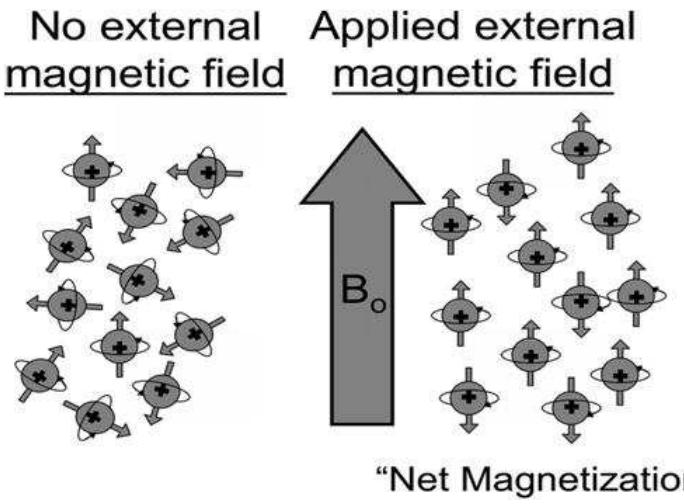

Figure 4.1. Alignment of protons with B_0 field. The absence of external magnetic field, hydrogen protons(+) are oriented randomly. When the protons are placed in a strong magnetic field (B_0), a net magnetization will be produced parallel to the main magnetic field [77].

resulting from an excitation of the spin system, M_z, occurs. The net magnetization M_z is proportional to the number of spins in that voxel. All of the longitudinal magnetization is flipped over and rotated into transverse magnetization by a radiofrequency (RF) pulse at the Larmor frequency. The amount of rotation relies on the strength and duration of the RF pulse. Therefore, magnetization lies in the xy-plane and M_z becomes M_{xy}. If we switches off RF field, the absorbed energy is retransmitted at the resonance frequency, which causes the spins to return to original longitudinal orientation. Furthermore, the precession begins to dephase. In other words, the system of dynamic equilibrium is observed. This process is called as a relaxation resulting from spin-lattice interaction and spin-spin interaction. The spin-spin interaction causes the decrease of the transverse components. Because of the different chemical environment,

the spins rotate at different angular frequencies, which is defined as spin-spin interactions. To illustrate; free protons in cerebrospinal fluid provide little dephasing and long spin-spin relaxation time. The spin-lattice interaction refers to as interactions of the spins with the surrounding macromolecules. The energy to the lattice gives rise to vibrations in the lattice. The spins return to their preferred lower energy state. As a result of this, the longitudinal component of the net magnetization reaches to its equilibrium value, which refers to as spin-lattice relaxation time (T_1). This relaxation time (T_1) depends on external magnetic field [78].

The external magnetic field which mentioned above, the magnetic field of MR system, is derived from large electric current flowing through wires that are formed into a loop in the magnet of imaging system. After immersing the wires in liquid helium, we obtain very large currents which lead to the strong magnetic field. Generally, the MR system has magnetic field the strength of 1.5-T (Tesla). Precession of the nuclei is related to the applied magnetic field. Therefore, we can mention about the concept of the Larmor frequency.

$$\omega_0 = \gamma_0 \cdot B_0 \tag{4.1}$$

where ω_0 is the Larmor frequency in megahertz (MHz) (the precessional frequency), γ_0 is the gyromagnetic ratio, and B_0 is the strength of the magnetic field in tesla (T) [77].

In summary, the signal derived from the transfer magnetization vector is optimized and it transforms into MRI images by Fourier analysis. The signal intensity or brightness on an MR image change according to the intrinsic features of biological tissue.

4.2. Image Reconstruction for Combined DOT-MRI

Magnetic resonance imaging possesses tissue discrimination in its high spatial resolution whereas DOT characterizes physiological properties of tissue. Considering these two important properties which belong to MRI and DOT, the combination of

the two measurement techniques has led to a new interest in cancer diagnosis.

In the literature, there are several important studies regarding combined DOT with other imaging techniques such as X-ray tomosynthesis [79], ultrasound [80], magnetic resonance imaging [81, 82]. Among these multi-modality imaging techniques, the combined DOT-MRI has become more effective and widespread in recent years. MRI imaging technique having a high spatial resolution contributes to DOT imaging modality having a high contrast resolution. Thus, researchers are able to obtain a complementary structural and a functional physiological information [83].

There have been a number of studies concerning the combined MR-DOT system. In particular, frequency domain near infrared DOT system is used in this combination. Initially, this hybrid system was used for cancer imaging in small animals. Subsequently, it has been used for breast cancer imaging. This technique is less expensive compared with other systems and effective in terms of separating absorption from scattering coefficients. In general, this optical imaging system is integrated with the 4 T MRI system. DOT system measures the amplitude and phase of detected signals by network analyzer. To illustrate, network analyzer allows modulation frequency between 100 MHz and 300 MHz. This system implements four different wavelength; 665 nm, 785 nm, 800 nm, and 830 nm [84].

In MRI-DOT combination, initial estimates of the optical properties for forward problem are chosen from MRI. Because optical properties of anatomical structures of breasts change female to female, estimation of the optical properties may not be accurate in the absence of MRI. To illustrate, Schweiger and Arridge demonstrated that the stability and convergence of imaging process are associated with initial estimates. The choice of correct initial guess contributes to image reconstruction [73]. Furthermore, the boundary of the tissue is irregular, so determination of this boundary condition is difficult. In order to tackle this difficulty, the mesh used for forward solver is generated from MRI. Thus, the mesh is formed via an accurate boundary condition derived from MRI. Additionally, biological tissue is the heterogenous. In other words, different tissue types are different from each other with respect to scattering and absorption

properties of them. The reconstruction of DOT does not provide this internal structure information. Conversely, MRI provides high spatial resolution because of having the property of excellent tissue discrimination. In this case, we can separate the mesh into regions according to different optical properties of tissue regions. After solving forward problem, an inverse problem is solved by minimizing objective the difference between modeled and measurement data which mentioned above. The solution is obtained in the similar way with the section named Tikhonov minimization. However, the regularization parameters are assigned according to regions which are segmented by a spatial resolution of MRI. In order to solve the inverse problem, dual mesh is used, which we discussed above sections.

Briefly, we can interpret this hybrid image procedure with the phantom experiments step by step. Initially, multi-modality phantom can be constructed. This phantom is divided into several regions. These regions simulate optical properties of tissue.

To illustrate, the phantom was divided into four regions; shell, background, irregular shape and 7 mm circular inclusion, which is shown in following Figure 4.2. After preparation this solid phantom, the MR image was used to determine not only the outer boundary information but also boundaries of the interior region of interests of the object. Thus, the finite element mesh was generated in Figure 4.3 for solving forward problem [84].

The majority of the researchers used different methods to calculate regularization parameter in the literature. One of them is

$$\lambda_i = \frac{(Tr(J^T J)_i)}{N} \frac{|(\chi_i)|}{|(\chi_1)|} \tag{4.2}$$

where Tr is the trace of a matrix, and N is the number of unknowns, χ_i is the norm of the error in the first iteration [85]. Selecting this regularization parameter in an each iteration is an efficient by this Equation 4.2 [86]. In this study, the finite element mesh was divided into two region; a background region and region of interest (tumor location). The initial optical parameters which belong to these two regions were de-

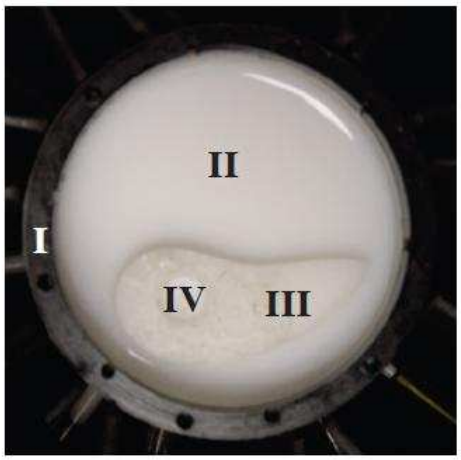

Figure 4.2. The picture of the multi-modality phantom [84].

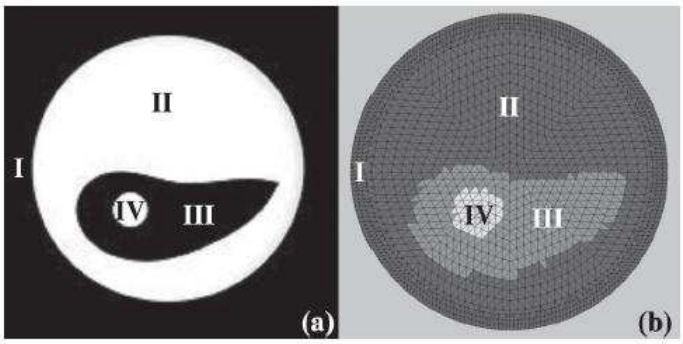

Figure 4.3. (a) The MR image of multi-modality phantom, (b)The FEM mesh used for the reconstruction program [84].

termined by nonlinear least squares estimate algorithm. In this case, the values of regularization parameters are modified;

$$\lambda_i = \frac{(Tr(J^T J)_i^r)}{N^r} \frac{norm(\chi_i)}{norm(\chi_1)}, \tag{4.3}$$

where r represents the region number, N^r is the number of unknowns related to that region.

5. DYNAMIC CONTRAST-ENHANCED DIFFUSE OPTICAL TOMOGRAPHY

An image acquired by applying a contrast agent is called as a dynamic contrast enhanced. In recent years, dynamic imaging has become a standard diagnostic tool in medicine. For example, extrinsic contrast agents are widely used in MRI as well as PET. Similarly, contrast agents in DOT play a critical role in localization of the tumor.

In particular, indocyanine green (ICG) is used in optical imaging studies. ICG is a clinical approved contrast agent, which was approved for human use by FDA in 1956. After administration of ICG, it binds to plasma proteins [87]. It has different properties from Gadolinium which is an MRI contrast agent. Gadolinium is a very small agent. Conversely, ICG Contrast agent is the substance which is used to enhance contrast between diseased and normal tissue. While ICG behaves like a low permeability agent, Gadolinium leaves the vasculature because of its molecular weight. The molecular weight of ICG (67 kD) is much greater than that of Gadolinium (0.57 kD). Therefore, distribution of ICG is intravascular. In the presence of ICG, we obtain additional information of vascular properties such as vascular volume and permeability. This information is associated with the rate of tumor growth. In essence, Nitziachristos *et al.* and Intes *et al.* demonstrated that ICG has different impact on benign and malignant tumors [33, 35].

ICG plays an important role in improvement of DOT. In essence, researchers have presented simulation studies in order to prove variability of the ICG kinetics between different case by using its pharmacokinetics [86]. Another significant study is using the multimodality contrast agents. In recent years, researchers have started to use bi-functional contrast agent in order to obtain information from DOT and MRI simultaneously. Thus, we get a functional and an anatomical information with a high sensitivity and a high spatial resolution. Additionally, researchers demonstrated DOT validation in the clinical trials for breast cancer via dual modality features of dynamic

DOT.

5.1. Modeling and Estimation of ICG Pharmacokinetics

Pharmacokinetics can be defined as a system of absorption and distribution of an administered drug. The rate of absorption and extraction in the body changes according to biological alternations. Therefore, imaging the pharmocokinetics rates is a significant means for tumor detection. The majority of scientists have been interested in the dynamic behavior of contrast agents. Essentially, Tofts employed pharmacokinetics models for analyzing dynamic contrast-enhanced T1-weighted data derived from MRI [88]. Similarly, this model has been used to reconstruct pharmacokinetic rate image of ICG. In this analysis, a compartmental modeling was used.

5.1.1. Two compartment model of ICG pharmacokinetics

Pharmacokinetics is the rate of change of ICG concentration in vascular tumors. In order to handle the ICG transition between different compartments, we use a compartmental model. In essence, ICG flows in tight capillaries of normal vessels. Furthermore, ICG may behave as diffusible flow in the leaky capillary of cancer vessels. In this case, we accept that tumor region is divided into two parts such as the plasma (intravascular) and extracellular extravascular space, (see Figure 5.1).

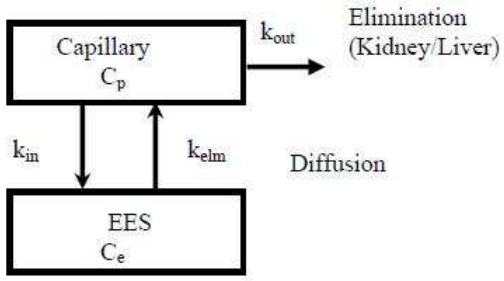

Figure 5.1. The representation of two-compartment model.

The rates of exchange between different compartments can be represented via coupled ordinary differential Equations 5.1 and 5.2. In these equations, coefficients are called as the pharmacokinetic rates.

$$\frac{dC_p(t)}{dt} = -(k_{in} + k_{elm})C_p(t) + k_{out}C_e(t), \tag{5.1}$$

$$\frac{dC_e}{dt} = k_{in}C_p(t) - k_{out}C_e(t) \tag{5.2}$$

where k_{elm} (min^{-1}), ν_p, ν_e, k_{in} (min^{-1}) and k_{out} (min^{-1}), C_p (μM) and C_e (μM) represent ICG elimination from the body through kidneys and livers, the plasma volume fraction, extracellular extravascular volume fractions, pharmacokinetic rates that depend on leakage into and drainage out of the EES, ICG concentration in plasma and EES respectively. If we use these two equations above, we are able to obtain the net flow from the plasma to the extravascular compartment and intravascular plasma;

$$C_p = A_1 \exp(-\alpha_1 t) + A_2 \exp(-\alpha_2 t) \tag{5.3}$$

where $A_1(\mu M)$ and $A_2(\mu M)$ represent amplitudes of exponential components. Additionally, $\alpha_1(s^{-1})$ and $\alpha_2(s^{-1})$ refer as their rate constants. This equation state that the net flow from the plasma to the compartment and kidney or liver can be indicated via a biexponential decay. In essence, we can express the total ICG concentration as a linear combination of the intravascular and the extravascular concentration;

$$C_t(t) = \nu_p C_p + \nu_e C_e, \tag{5.4}$$

$$C_t(t) = A_1(\nu_p + \frac{k_{in}}{k_{out} - \alpha_1}) \exp(-\alpha_1 t) + A_2(\nu_p + \frac{k_{in}}{k_{out} - \alpha_2}) \exp(-\alpha_2 t) \\ -(A_1(\frac{k^{in}}{k^{out} - \alpha_1}) + A_2(\frac{k_{in}}{k^{out} - \alpha_2})) \exp(-k_{out} t). \quad (5.5)$$

Here, the permeability surface areas, k_{in} (min^{-1}) and $k_{out}(min^{-1})$, are defined with this following equation. $k_{in} = P_i S_i \rho_i$ and $k_{out} = P_o S_o \rho_o$ where P_i and P_o, S_i and S_o, ρ_i and ρ_o represent the capillary permeability contrast (in centimeters per second), the capillary surface area (in square centimeters), the tissue density (in grams per cubic centimeters) respectively. Note that the plasma volume fraction, v_p, is calculated by hematocrit (Hct) and the Hb concentration in the red blood cells [89];

$$(\frac{Hb_T}{Hb_B})(\frac{100 - Hct}{Hct}) \approx 2.415 \times 10^{-4} \times Hb_T(\mu M). \quad (5.6)$$

Additionally, we can express this following equation concerning the relationship between transmission and absorbance such that

$$A = -\log_{10}^{T}. \quad (5.7)$$

Here, the an absorbance of medium and a transmission through a medium are defined as $A = \epsilon C d$ and $T = exp(-\mu_a d)$ respectively. With the help of these three equations, an absorption coefficient is written as $\mu_a = \epsilon c \ln 10$. Thus, we are able to define that absorption coefficient is proportional to a concentration and an extinction coefficient of ICG such that

$$\mu_a = 2.3 \epsilon C. \quad (5.8)$$

According to this Equation 5.8, the change in the absorption coefficient which is caused by the injected ICG concentration, is given by

$$\delta \mu_a = 2.3 \epsilon \delta C, \quad (5.9)$$

where ϵ and C represent the extinction coefficient and concentration of ICG respectively. M. Burçin Ünlü [36] used six simulations and demonstrated that ICG kinetics curves are the significant tool for tumor characterizations. In this study, six simulations which have different situations in terms of tumor locations were used. ICG concentrations were calculated via the equation which was obtained by using pharmacokinetics model. In this equation, the values of the psychological parameters, $k_{in}, k^{out}, A_1, A_2, \nu_p, \alpha_1, \alpha_2$, were chosen from the article which belongs to David J. Cucia *et al.* [89]. Then, the ICG curves were obtained. In this case, the concentration of ICG may be called as a calculated concentration of ICG [86]. Furthermore, he got information about absorption maps of tissue by the theory of image reconstruction. While an absorption coefficient at each time point changes, the change in scattering is ignorable owing to ICG. After using the optical property of tissue, the absorption coefficient, he obtained ICG concentration via Equation 5.9. Here, this value may be called measured concentration of ICG reconstruction. In this step, nonlinear least squares techniques was applied, which enabled accuracy of the ICG dynamic parameters. Thus, the accuracy of recovered ICG dynamics parameters provide us with tumor characterization. Thanks to the pharmacokinetic model, he showed that ICG kinetic curves increase the spatial resolution.

On one hand some researchers have interested in absorbance characteristics of ICG for DOT, on the other hand, others have used fluorescence characteristics of ICG for DOT [90].

5.2. A Multimodal Contrast Agent for Simultaneous Magnetic Resonance and Optical Imaging of Small Animals

M. B. Ünlü *et al.* [86] used combined diffuse optical tomography and 4T magnetic resonance (MR) scanner simultaneously to measure the kinetics of the a contrast agent in vivo small animal. Initially, a phantom which has similar optical properties with the small animal was constructed and was obtained measurement by DOT. By this way, some errors resulting from systematic variations between source-detector readings were eliminated. Without running MRI, the static absorption and the scattering maps could

be obtained by DOT, which was mentioned above sections. In the presence of MRI, T_2 weighted MRI scanning was obtained and provided us with determination of the location source and detectors of DOT. Furthermore, T_1 weighted images derived from MRI contributes to an extraction of the boundary conditions of tumor. According to this information, the finite element mesh was divided into two regions; the tumor and non-tumor regions.

These two static sets of MRI, T_1 and T_2 weighted images, are crucial to determine the location of tumor and internal organs. After administration contrast agents with bi-functional contrast agent enhancement, MRI and DOT dynamic curves and the reconstructed optical absorption maps were obtained. In this step, bi-functional plays an important role on obtaining DOT and MRI images simultaneously. As a result of this study, he obtained the enhancement maps of the small animal study after the injection of the contrast agent bi-functional agent, (see Figures 5.2 and 5.3).

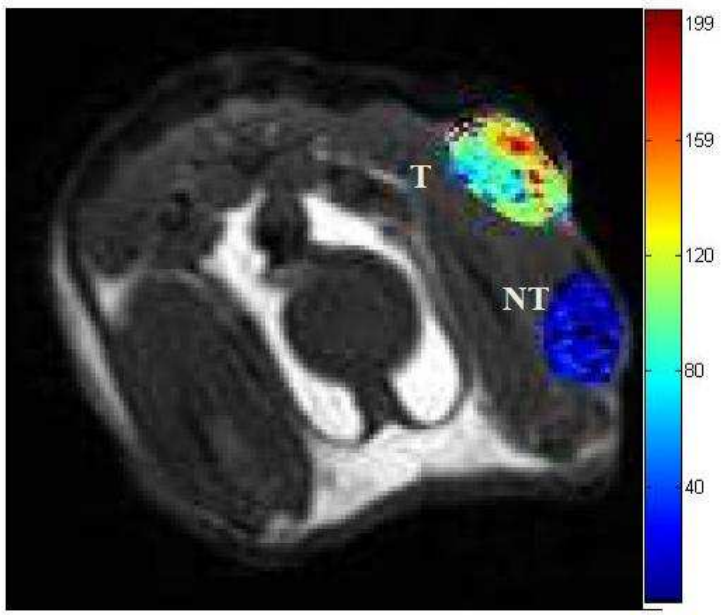

Figure 5.2. Enhancement image is given. T_1- weighted MR image at the peak signal enhancement overlaid on the anatomical image. The tumor is denoted with the label T. The label NT denotes the non-tumor region [36].

Furthermore, bi-functional contrast enhancements which were obtained by DOT and MRI demonstrated that the peak enhancement in tumor region was higher than

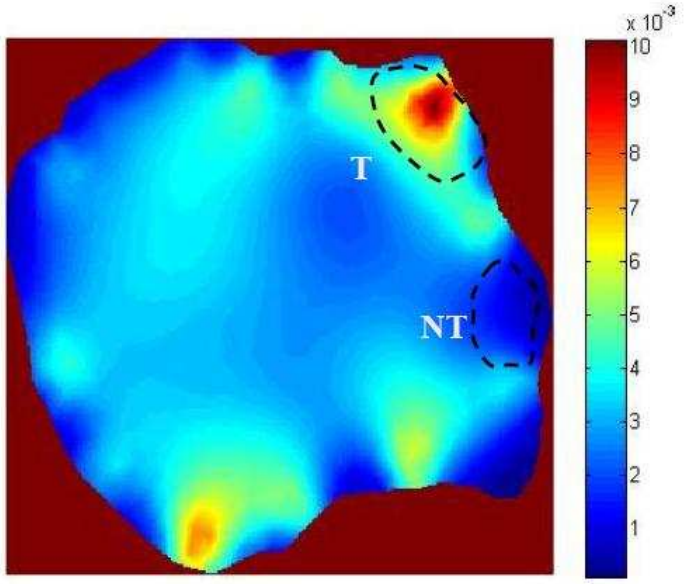

Figure 5.3. Enhancement image is given. The reconstructed peak absorption enhancement is given. The tumor and the non-tumor regions are labeled on the both image [36].

the non-tumor region.

These two Figures 5.4 and 5.5 showed that the peak enhancement in the tumor region was higher compared with non-tumor region. Finally, the results enabled to compare bi-functional contrast agent kinetics detected by the MRI and DOT systems in tumor, (see Figure 5.6).

In other words, this study demonstrated that multimodal imaging provided molecular, functional and anatomical information with a high sensitivity and a high spatial resolution [36].

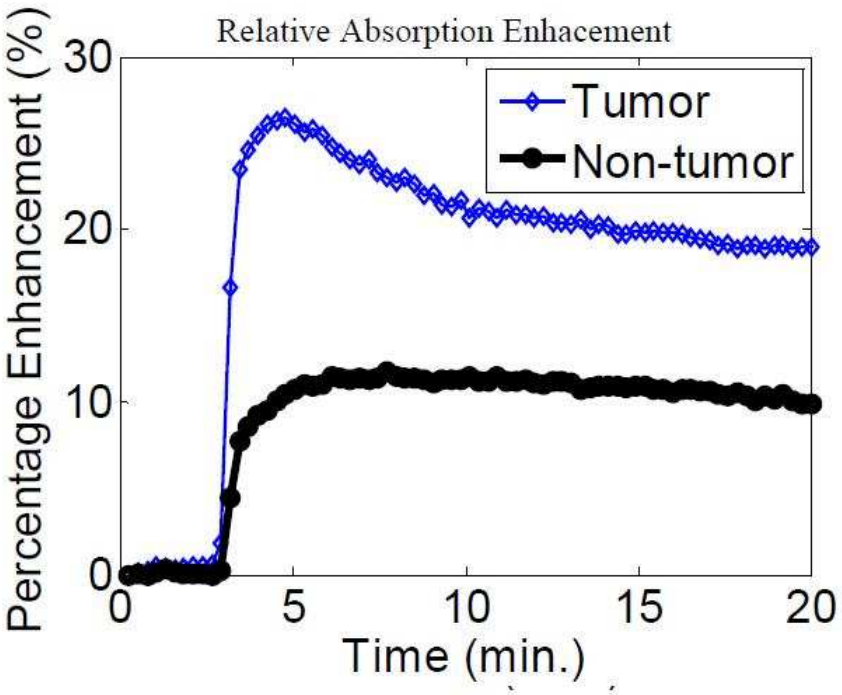

Figure 5.4. Curves showing the change in bi-functional contrast agent concentration that is measured by the DOT system. The peak enhancement occurs at 4.8 minutes. The tumor and the non-tumor regions show different enhancement kinetics [36].

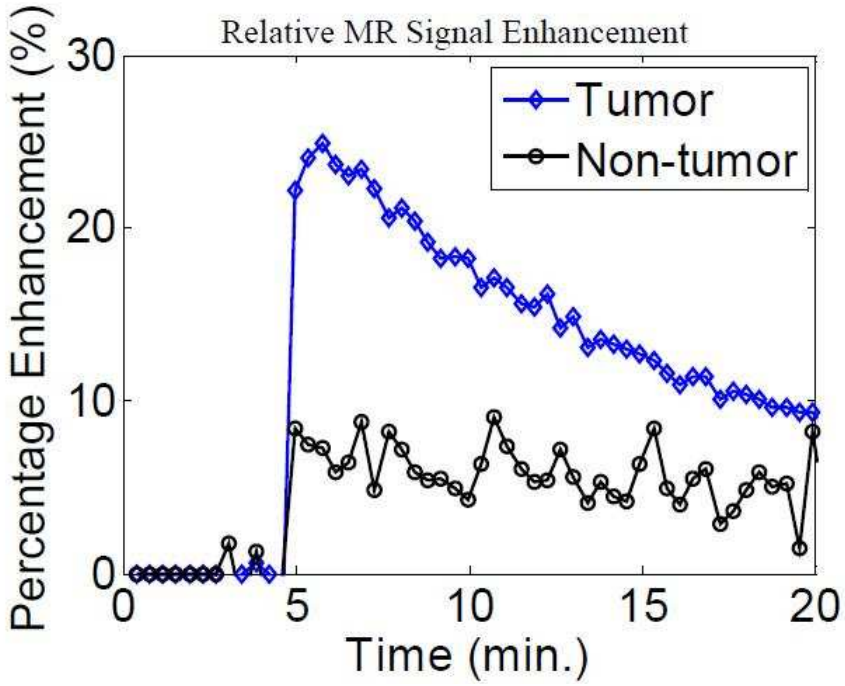

Figure 5.5. The MRI shows the change in bi-functional contrast agent concentration that is measured by the MRI system. The peak enhancement occurs at 5.2 minutes. The tumor and the non-tumor regions shows different enhancement kinetics [36].

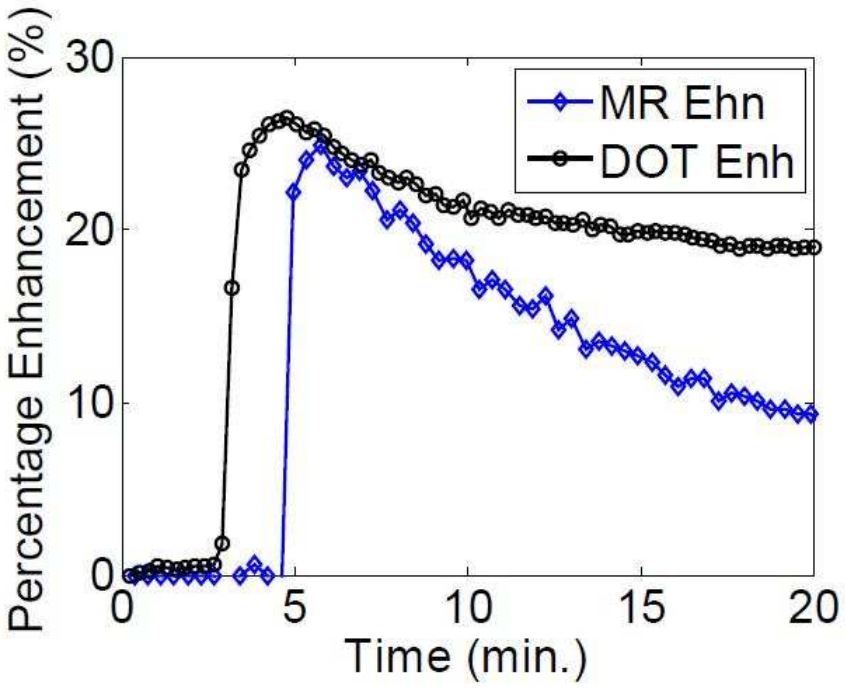

Figure 5.6. The comparison of bi-functional contrast agent kinetics detected by the MRI and the DOT system in the tumor. The DOT measurements are more sensitive than the MRI measurements [36].

6. CONCLUSION

It is a clear that DOT gives an information about major changes in the distribution of absorption and scattering coefficients within the region of interest. However, we have discussed that its spatial resolution is low, because the inverse model of its is ill-posed. Even though it has a poor spatial resolution, we can alleviate this undesirable property with priori information derived from other modalities. In this case, the combined DOT and MRI is the significant hybrid model. While MRI contributes to DOT in terms of an anatomical information, DOT enables composition and metabolism information. Although there are greatest recent progress in demonstration of clinical application, improvements in DOT are necessary for qualitative and quantitative accuracy considering clinical applications. Especially, a number of researchers demonstrated the validation of DOT by comprehending distribution of ICG in human breast, and they have compared it with MRI. In this case, MRI is called as "Gold Standard" for the fidelity of DOT in the clinical environment. Furthermore, using multimodality imaging probes like bi-functional probes enables us to compare images and parameters derived from MRI and DOT accurately, simultaneously. According to these types of studies, DOT has the capability of localization and quantification of exogenous tissue chromophore concentrations. Furthermore, we can indicate that we can determine the region of suspicious lesions by using DOT after the administration of ICG. Thus, this hybrid model gives a complementary information and contributes to characterization of tumor. Considering a number of studies, we can point that improved image quality for DOT is accomplishable. Taking into consideration, this technique enables functional imaging of biological tissue, so researchers have interested in the improvement of DOT. In this regard, studies concerning experimental methods and instrumentation of DOT and new theoretical techniques applied to modeling and image reconstruction for DOT are necessary worldwide.

REFERENCES

1. Cutler, M., "Transillumination as Aid in The Diagnosis of Breast Lesions", *Surgery, Gynecology, Obstetrics*, Vol. 48, pp. 721-729, 1929.

2. Jobsis, F. F., "Noninvasive Infra-red Monitoring of Cerebral and Myocardial Sufficiency and Circulatory Parameters", *Science*, Vol. 198, pp. 1264-1267, 1997.

3. Fabrizio, M., D. Bianco, A. Ismaelli, G. Zaccanti, *Light Propagation Through Biological Tissue and Other Diffuse; Media Theory Solutions and Sottware*, The Society of Photo-optical Instrumentation Engineers, 2010.

4. Hollis, V., *Non-Invasive Monitoring of Brain Tissue Temperature by Near-Infrared Spectroscopy*, P.h.D. Thesis, University College London, 2002.

5. Niemz, H. M., *Laser Tissue Interaction*, Springer-Verlang Berlin Heidelberg, 1996.

6. Cheong, W. F., S. A. Prathl, "A Review of the Optical Properties of Biological Tissues", *Institute of Electrial and Electronics Engineers, Journal of Quantum Electronics*, Vol. 26, No. 12, pp. 2166-2185, 1990.

7. Hillman, M. C. E., *Experimental and Theoretical Investigations of Near Infared Tomographic Imaging Methods and Clinical Applications*, P.h.D. Thesis, University College London, 2002.

8. Barret, H. H., *Radiological Imaging-Detection and Processing*, Academic Press, New York, 1981.

9. Vaupel, P., F. Kallinowski, P. Okunieff, "Blood Flow, Oxygen and Nutrient Supply, and Metabolic Microenvironment of Human Tumors : A Review", *Cancer Research*, Vol. 49, pp. 6449-6465, 1989.

10. Profio, A. E., G. A. Navarro, O. W. Sartorius, "Scientific Basis of Breast Diaphanography", *Medical Physics.*, Vol. 16, pp. 60-65, 1989.

11. Pogue, B. W., S. Jiang, S. Srinivasan, X. Song, 2004, " Near-infrared Scattering Spectrum Differences Between Benign and Malignant Breast Tumors Measured in vivo with Diffuse Tomography", Biomedical Topical Meetings, *The Optical Society of America*, March 5, Washington.

12. Hielscher, A. H., J. R. Mourant, and I. J Bigio, "Influence of Particle Size and Concentration on the Diffuse Backscattering of Polarized Light from Tissue Phantoms and Biological Cell Suspensions", *Optical Society of America*, Vol. 36, pp. 125-135, 1997.

13. Pogue, B. W., S. P. Poplack, T.O. McBride, W. A. Wells, "Quantitative Hemoglobin Tomography with Diffuse Near-Infrared Spectroscopy: Pilot Results in the Breast", *Radiology*, Vol. 218, pp. 261-266, 2001.

14. Hebden, J. C., A. Gibson, R. M. Yusof, N. Everdell, E. M. C. Hillman, David T. D., Simon R A., T. Austin, J. H. Meek and J. S Wyatt, "Three-Dimensional Optical Tomography of The Premature Infant Brain", *Physics in medicine and biology*, Vol. 47, pp. 4155-4166, 2002.

15. Dehghani, H. and D. T. Delpy, "Near Infared Spectroscopy of the Adult Head: effect of scattering and absorbing abstructions in the cerebrospinal fluid layer on light distribution in the tissue", *Optical Society Of America* , Vol. 39, pp. 4721-4729, 2000.

16. Hebden, J. C., and D. T. Delpy, Diagnostic imaging with light, *British Journal of Radiology*, Vol. 70, pp. S206-S214, 1997.

17. Arridge, S. R., and J. C. Hebden, "Optical Imaging in Medicine: II. Modelling and Reconstruction", *Physics in Medicine and Biology*, Vol. 42, pp. 841-853, 1997.

18. Chance, B., J. S. Leigh, H. Miyake, D. S. Smith, S. Nioka, R. Greenfeld, M. Finander, K. Kaufmann, W. Levy, M. Young, P. Cohen, H. Yoshîka, and R. Boretsky "Comparison of Time-Resolved and Unresolved Measurements of Deoxyhemoglobin in Brain", *Proceedings of the National Academy of Sciences of the United States of America*, Vol. 85, pp. 4971-4975, 1988.

19. Patterson, M. S., B. Chance, B. C. Wilson, "Time resolved reflectance and transmittances for the non-invasive Measurement of Tissue Optical Properties", *Applied Optics*, Vol. 28, pp. 2331-2336, 1989.

20. Fishkin, J. B., E. Gratton, W. W. Mantulin, "Diffusion of Intensity Modulated Near Infrared Light in Turbid Media", *Proceedings of The Society of Photo-optical Instrumentation Engineers*, Vol. 1431, pp. 122-135, 1991.

21. Patterson, M. S., J. D. Moulton, B. C. Wilson, K. W. Berndt, and J. R. Lakowicz "Frequency-Domain Reflectance for the Determination of the Scattering and Absorption Properties of Tissue", *Applied Optics*, Vol. 30, pp. 4474-4476, 1991.

22. McBride, T. O., B. W. Pogue, E. D. Gerety, S. B. Poplack, U. L. Osterberg, and K. D. Paulsen, "Spectroscopic Diffuse Optical Tomography for Quantitatively Assessing Hemoglobin Concentration and Oxygenation in Tissue", *Applied Optics*, Vol. 38, pp. 5480-5490, 1999.

23. Ishimaru, A., *Wave Propagation and Scattering in Random Media*, Academic Press, Inc., New York, 1978.

24. Singer, J. R., F. A. Grunbaum, P. D. Kohn, J. P. Zubelli, "Image Reconstruction of the Interior of Bodies that Diffuse Radiation", *Science*, Vol. 248, pp. 990-993, 1990.

25. Arridge, S. R., Scheiger M., Delpy, D. T., "Iterative Reconstruction of Near Infrared Absorption Images", *The International Society for Optics and Photonics*, Vol. 1767, pp. 372-383, 1992.

26. Arridge, S. R., M. Schweijer, M. Hiraoka, and D. T. Delpy, "A Finite Element Approach for Modeling Photon Transport in Tissue", *Medical Physics*, Vol. 20, pp. 299-308, 1993.

27. Schweiger, M., *Application of the Finite Element Method in Infrared Image Reconstruction of Scattering Media*, P.h.D. Thesis, University of London, 1994.

28. Schmidt, F. E. W., *Development of a Time-Resolved Optical Tomography System for Neonatal Brain Imaging*, P.h.D. Thesis, University College London, 1999.

29. Dehghani, H., B. W. Pogue, S. P. Poplack, and K. D. Paulsen, "Multiwavelength Three-Dimensional Near-Infrared Tomography of the Breast: Initial Simulation, Phantom, and Clinical Results", *Applied Optics*, Vol. 42, No. 1, pp. 135-145, 2003.

30. Schweiger, M., S. R. Arridge, "Optical Tomographic Reconstruction in a Complex Head Model Using a Priori Region Boundary Information", *Physics in Medicine Biology*, Vol. 44, pp. 2703- 2721, 1999.

31. Pogue, B. W., and K. D. Paulsen, "High Resolution Near Infrared Tomographic Imaging Simulations of Rat Cranium Using a Priori MRI Structural Information", *Optics Letters*, Vol. 23, No. 21, pp. 1716-1718, 1998.

32. Dehghani, H., B. W. Pogue, J. Shudong, B. Brooksby, and K. D. Paulsen, "Three Dimensional Optical-tomography: Resolution in Small-Object Imaging", *Applied Optics*, Vol. 42, No. 16, pp. 3117-3128, 2003.

33. Ntziachristos, V., A. G. Yodh, M. Schnall and B. Chance, "Concurrent MRI and Diffuse Optical Tomography of Breast After Indocyanine Green Enhancement", *Proceedings of the National Academy of Sciences of the United States of America*, Vol. 97, pp. 2767-2772, 2000.

34. Ntziachristos, V., A. G. Yodh, M. D. Schnall and B. Chance , "MRI-guided Diffuse

Optical Spectroscopy of Malignant and Benign Breast Lesions Neoplasia", *Neoplasia*, Vol. 4, pp. 347-54, 2002.

35. Intes, X., J. Ripoll, Y. Chen, S. Nioka, A. G. Yodh, and B. Chance, "In vivo Continuous-Wave Optical Breast Imaging Enhanced with Indocyanine Green", *Medical Physics*, Vol. 30, pp. 1039-47, 2003.

36. Ünlü, M. B., Y. Lin, B. Grimmond, A. Sood, E. Uzgiris, O. Nalcioglu, and G. Gulsen, Tu and Yuen, "A Multimodal Contrast Agent for Simultaneous Magnetic Resonance and Optical Imaging of Small Animal", *Proceedings of the International Society for Optics and Photonics*, Vol. 7557, pp. 75570C-75570C-7, 2010.

37. Bastiaens, P. I. and A. Squire, "Fluorescence Lifetime Imaging Microscopy: Spatial Resolution of Biochemical Processes in the Cell" , *Trends in Cell Biology*, Vol. 9, pp. 48-52, 1999.

38. Kuwana, E. and E. M. Sevick-Muraca, "Fluorescence Lifetime Spectroscopy for pH Sensing in Scattering Media", *Analytical Chemistry*, Vol. 75, pp. 4325-4329, 2003.

39. Yavari, N., *Optical Spectroscopy for Tissue Diagnostics and Treatment Control*, P.h.D. Thesis, University of Bergen, 2006.

40. Patterson, M. S., B. C. Wilson, and D. R. Wyman, "The Propagation of Optical Radiation in Tissue I. Models of Radiation Transport and Their Application", *Lasers in Medical Science*, Vol. 6, pp. 155-168, 1990.

41. Jacques, S., M. S. Patterson, "Light-tissue Interactions", *In: Webb CE, Jones J.D.C., Handbook of laser technology and applications, Institute of Physics Publishing*, pp. 1955-1993, 2004.

42. Arridge, S. R., " Optical Tomography in Medical Imaging", *Inverse Problems*, Vol. 15, pp. R41-R93, 1998.

43. Wang, Lihong V., H. Wu, *Biomedical Optics Principles and Imaging*, Sons, Inc., Hoboken, New Jersey, 2007.

44. Wilson, B. C., G. Adam, "A Monte Carlo Model for the Absorption and Flux Distributions of Light in Tissue", *Medical Physics*, Vol. 10, pp. 824-830, 1983.

45. Culver, J. P., R. Choe, M. J. Holboke, L. Zubkov, T. Durduran, A. Slemp, V. Ntziachristos, B. Chance, and Yodh A. G., "Three-Dimensional Diffuse Optical Tomography in the Parallel Plane Transmission Geometry: Evaluation of a Hybrid Frequency Domain/Continuous Wave Clinical System for Ireast imaging", *Medical Physics*, Vol. 30, pp. 235-246, 2003.

46. Hielscher, A. H., A. D. Klose, A. K. Scheel, B. Moa-Anderson, M. Backhaus, U. Netz, and J. Beuthan, "Sagittal Laser Optical Tomography for Imaging of Rheumatoid Finger Joints", *Physcis in Medicine and Biology*, Vol. 49, pp. 1147-1163, 2004.

47. Ren, K., G. S. Abdoulaev, G. Bal, A. H. Hielscher, "Algorithm for Solving the Equation of Radiative Transfer in the Frequency Domain", *Optics Letters*, Vol. 29, pp. 578-580, 2004.

48. Ripoll, J., and V. Ntziachristos, "Iterative Boundary Method for Diffuse Optical Tomography", *Journal of Optical Society of America*, Vol. 20, pp. 1103-10, 2003.

49. Heino, J., S. R. Arridge, J. Sikora and E. Somersalo, " Anisotropic Effects in Highly Scattering Media", *Physical Review E* , Vol. 68, pp. 031901 − 0319018 , 2003.

50. Arridge, S. R., M. Cope, D. T. Delply, M. Cope, and D. T. Delpy, " The Theoretical Basis for the Determination of Optical Pathlengths in Tissue The Theoretical Basis for the Determination of Optical Pathlengths in Tissue: Temporal and Frequency Analysis", *Physics in Medicine and Biology*, Vol. 37, pp. 1531-1560, 1992.

51. Schweiger, M., S.R. Arridge, M. Hiraoka, D. T. Delpy, "The Finite Element Model for the Propagation of Light in Scattering Media: Boundary and Source Conditions",

Medical Physics, Vol. 22, pp. 1779-1792, 1995.

52. Arridge, S. R., "Optical Tomography in Medical Imaging", *Inverse Problem*, Vol. 15, pp. R41-R93, 1999.

53. Dehghani, H., S. Srinivasan, B. W. Pogue, A. Gibson, "Numerical Modelling and Image Reconstruction in Diffuse Optical Tomography", *Philpscophical Transactions of The Royal Society*, Vol. 367, pp. 3073-3093, 2009.

54. Ünlü, M. B., Ö. Birgül, R. Shafiiha, G. Gülsen, and O. Nalcıoğlu, "Diffuse Optical Tomographic Reconstruction using Multifrequency Data", *Journal of Bimedical Optics*, Vol. 11, No. 5, pp. 0540081 − 0540088, 2006.

55. Schweiger, M., S. R. Arridge, M. Hiraoka, and D. T. Delpy, "The Finite Element Method for the Propagation of Light in Scattering Media: Boundary and Source Conditions", *Medical Physics*, Vol. 22, No. 11, pp. 1179-1792, 1995.

56. Heino, J., and E. Somersalo, "Estimation of Optical Absorption in Anisotropic Background", *Inverse Problem*, Vol. 18, pp. 559-573, 2002.

57. Tarvainen, T., "Computational Methods for Light Transport in Optical Tomography", *Natural and Environmental Sciences*, Vol. 199, p. 123, 2006.

58. Yalavarth, P. K. and B. W., H. Dehghani, K. D. Paulsen, "Weight- Matrix Structured Regularization Provides Optimal Generalized Least-Squares Estimate in Diffuse Optical Tomography", *American Association of Physicists in Medicine* , Vol. 34, pp. 2085-2098, 2007.

59. Bertero, M. and P. Boccacci, "Introduction to Inverse Problem in Imaging", *The Institute of Pysics, London*, 1998.

60. Choe, R., *Diffuse Optical Tomography and Spectroscopy of Breast Cancer and Fetal Brain*, P.h.D. Thesis, the University of Pennsylvania in Partial, 2005.

61. Ntziachristos, V., *Concurrent Diffuse Optical Tomography, Spectroscopy and Magnetic Resonance Imaging of Breast Cancer*, P.h.D. Thesis, the University of Pennsylvania in Partial, 2000.

62. Deghani, H., M. E. Eames, P. K. Yalavarthy, S. C. Davis, S. Srinivasan, C. M. Carpanter, B. W. Pogue, and K. D. Palsen, "Near Infared Optical Tomography Using NIRFAST: Algorithm for Numerical Model and Image Reconstruction", *Common Numerber Methods Engineering*, Vol. 25, No. 16, pp. 711-732, 2008.

63. Arridge, S. R., "Photon Measurement Density Function, Part 2: Finite Element-Method Calculations", *Applied Optics*, Vol. 34, No.34, pp. 8026-8037, 1995.

64. Brooksby, B. A., *Combining Near Infrared Tomography and Magnetic Resonance Imaging to Improve Breast Tissue Chromophore and Scattering Assesment* , P.h.D. Thesis, Tayer School of Enginering Darmouth College Hanover, 2005.

65. Penrose, R., "A Generalized Inverse For Matrices", *University of Cambridge*, pp. 406-413, 1995.

66. Fang, Q., *Computatioanal Methods for Microwave Medical Imaging*, P.h.D. Thesis, Thayer School of Engineering Darmouth College, 2004.

67. Ren, K., B. Moa-Anderson, G. Bal, X. Gu, and A. H. Hielscher, "Frequency Domain Tomography in Small Animals with the Equation of Radiative Transfer", *Society for Industrial and Applied Mathematics, Journal on Scientific Computing*, Vol.28, pp. 1463-1489, 2006.

68. Chance, B., M. Cop, E. Gratton, N. Ramanujam, and B. Tromberg, "Phase Measurement of Light Absorption and Scatter in Human Tissue", *Review of Scientific Instruments*, Vol. 69, pp. 3457-3481, 1998.

69. Barbour, R. L., H. L. Graber, Y. Pei, S. Zhong, and C. H. Schmitz, " Optical Tomographic Imaging of Dynamic Features of Dynamic Feature of Dense-Scattering

Media", *Journal of Optical Society of America*, Vol. 18, No. 12, pp. 3018- 3036, 2001.

70. Schweiger, M., and S. R. Arrige, "Optical Tomograhic Reconstruction in Complex Head Model Using a Priori Region Boundary Information", *Physics in Medicine and Biology*, Vol. 44, pp. 2703-2721, 1999.

71. Ntziachristos, V., A. G. Yodh, M. D. Schnall, and B. Chance, "MRI-Guided Diffuse Optical Spectroscopy of Malignant and Benign Breast Lesions", *Neoplasia* , Vol. 4, pp. 347-354, 2002.

72. Pogue, B. W., and K. D. Paulsen, "High Resolution Near-Infared Tomographic Imaging Simulations of of the Rat Cranium by Use of a Priori Magnetic Resonance Imaging Structural Information", *Optics Letters*, Vol. 23, pp. 1716-1718, 1998.

73. Brooksby, B., H. Dehghani, B. W. Pogue, and K. D. Paulsen, "Near Infared Tomography Breast Image Reconstruction with a Priori Structural Information from MRI: Algorithm Development for Reconstructing Heterogeneities", *Selected Topics in Quantum Electronics, Institute of Electrial and Electronics Engineers*, Vol. 9, pp. 199-209, 2003.

74. Yalavarthy, P. K., B. W. Pogue, H. Deghani, C. M. Carpenter, S. Jiang, and K. D. Paulsen, "Structural Information within Regularization Matrices Improves Near Infared Diffuse Optical Tomography", *Optical Society of America*, Vol. 15, pp. 8043-8058, 2007.

75. Tromberg, B. J., O. Coquoz, J. B. Fishkin, T. Pham, E. R. Anderson, J. Butler, M. Cahn, J. D. Gross, V. Venugopalan, and D. Pham, "Non-Invasive Measurements of Breast Tissue Optical Properties Using Frequency-Domain Photon Migration", *The Royal Society*, Vol. 352, pp. 661-668, 1997.

76. Suetens P., *Fundamentals of Medical Imaging*, Cambridge University Press, 2002.

77. Pooley, R. A., "Fundamental Physics of MR Imaging", *RadioGraphics* , Vol. 25,

pp. 1087-1099, 2005.

78. Weishaupt, D., D. Victor Kchli, M. Borut, *How does MRI Work?: An Introduction to the Physics and Function of Magnetic Resonance Imaging*, Springer-Verlag Berlin Heidelberg, 2003.

79. Li, A., E. L. Miller, M. E. Kilmer, T. J. Brukilaccio, T. Chaves, J. Stott, Q. Zhang, T. Wu, M. Choriton, R. H. Moore, D. B. Kopans, and D. A. Boas, "Tomographic Optical Breast Imaging Quided by Three-Dimensional Mammography", *Applied Optics*, Vol. 42, pp. 5181-5190, 2003.

80. Q. Zhu, S. H Kurtzman, P. Hedge, S. Tannenbaum, M. Kane, M. Huang, N. G. Chen, B. Jagjivan, and K. Zarfos, "Utilizing Optical Tomography with Ultrasound Localization to Image Heterogeneous Hemoglobin Distribution in Large Breast Cancers", *Neoplasia* , Vol. 7, No. 3, pp. 263-270, 2005.

81. Pogue, B. W., H. Zhu, C. Nwaigwe, T. O. McBride, U. L. Osterberg, K. D. Paulsen, and J. F. Dunn, *Hemoglobin Imaging with Hybrid Magnetic Resonance and Near-Infrared Diffuse Tomography, in: Oxygen Transport to Tissue XXI*, Kluwer Academic/Plenum Publisher, 2003.

82. Gültekin, G., H. Yu, J. Wang, O. Nalcioglu, S. Merritt, F. Bevilacqua, F. Bevillacqua, A. J. Durkin, D. J. Cuccia, R. Lanning, B. J. Tromberg, "Congruent MRI and Near-infrared Spectroscopy for Functioanl and Structural Imaging Of Tumors", *Technology in Cancer Research and Treatment*, Vol.1, pp. 497-505, 2002.

83. Merritt, S., F. Bevilacqua, A. J. Durkin, D. J. Cucia, R. Lanning, B. J. Tromberg, G. Gulsen, H. Yu, J. Wang, and O. Nalcioglu, "Coregistration of Diffuse Optical Spectroscopy and Magnetic Resonance Imaging in a Rat Tumor Model", *Applied Optics*, Vol. 42, pp. 2951-2959, 2003.

84. Gülsen, G., Ö. Birgül, M. B. Ünlü, R. Shafiiha, and O. Nalcioglu, "Combined Diffuse Optical Tomography (DOT) and MRI System for Cancer Imaging in Small

Anmals", *Techonology in Cancer Research and Treatment*, Vol.5, No. 4, pp. 351-363, 2006.

85. Franchois, A., and C. Pichot, "Microwave Imaging-Complex Permittivity Reconstruction with a LevenbergMarquardt Method", *Institute of Electrial and Electronics Engineers Antennas Propagation*, Vol. 45, pp. 203-15, 1997.

86. Ünlü, M. B., Ö. Birgül, and G. Gülsen, "A simulation Study of the Variability of Indocyanine Green Kinetics and Using Structural a Priori Information in Dynamic Contrast Enhanced Diffuse Optical Tomography", *Physics In Medicine and Biology*, Vol. 53, pp. 3189-3200, 2008.

87. Yoneya, S., T. Saito, Y. Komatsu, I. Koyama, K. Takahashi, and J. Duvoll-Young, "Binding Properties of Indocyanine Green in Human Blood", *Investigate Ophtalmology and Visual Science*, Vol. 39, pp. 1286-1290, 1998.

88. Tofts, P. S., and A. G. Kermode, "Measurement of the Blood-Brain Barrier Permeability and Leakage Space Using Dynamic MR Imaging: 1. Fundamental Concepts", *Magnetic Resonance in Medicine*, Vol.17, pp. 357-367, 1991.

89. Cuccia, D. J., F. Bevilacqua, A. J. Durkin, S. Merritt, B. J. Tromberg, G. Gulsen, H. Yu, J. Wang, and O. Nalcioglu, "In Vivo Quantification of Optical Contrast Agent Dynamics in Rat Tumors by Use of Diffuse Optical Spectroscopy with Magnetic Resonance Imaging Coregistration", *Applied Optics*, Vol. 42, pp. 294050, 2003.

90. Corlu, A., R. Choe, T. Durduran, M. A. Rosen, M. Scweiger, S. R. Arridge, M. D. Schnall, A. G. Yodh, "Three-Dimensional in Vivo Fluorescence Diffuse Optical Tomography of Breast Cancer In Humans", *Optic Express* , Vol. 15, No. 11, pp. 6696-6716, 2007.